A Control-Theoretic Perspective on BBR/CUBIC Congestion-Control Competition

Simon Scherrer[a], Adrian Perrig[a], Stefan Schmid[b]

[a] *Department of Computer Science, ETH Zürich, Switzerland*
[b] *Faculty IV - Electrical Engineering and Computer Science, TU Berlin, Germany*

arXiv:2510.22773v1 [cs.NI] 26 Oct 2025

Abstract

To understand the fairness properties of the BBR congestion-control algorithm (CCA), previous research has analyzed BBR behavior with a variety of models. However, previous model-based work suffers from a trade-off between accuracy and interpretability: While dynamic fluid models generate highly accurate predictions through simulation, the causes of their predictions cannot be easily understood. In contrast, steady-state models predict CCA behavior in a manner that is intuitively understandable, but often less accurate. This trade-off is especially consequential when analyzing the competition between BBR and traditional loss-based CCAs, as this competition often suffers from instability, i.e., sending-rate oscillation. Steady-state models cannot predict this instability at all, and fluid-model simulation cannot yield analytical results regarding preconditions and severity of the oscillation.

To overcome this trade-off, we extend the recent dynamic fluid model of BBR by means of control theory. Based on this control-theoretic analysis, we derive quantitative conditions for BBR/CUBIC oscillation, identify network settings that are susceptible to instability, and find that these conditions are frequently satisfied by practical networks. Our analysis illuminates the fairness implications of BBR/CUBIC oscillation, namely by deriving and experimentally validating fairness bounds that reflect the extreme rate distributions during oscillation. In summary, our analysis shows that BBR/CUBIC oscillation is frequent and harms BBR fairness, but can be remedied by means of our control-theoretic framework.

1. Introduction

During the global deployment of the BBR congestion-control algorithm (CCA) [8], researchers have documented several cases of unexpected BBR behavior, all with significant implications on performance and fairness [16, 19, 36, 43, 44, 49]. To improve the safety of CCA deployment in the future, recent research has aimed at a more fundamental understanding of BBR based on *modeling*, i.e., mathematical descriptions that enable insights valid for a wide range of network settings.

This model-based work has taken two different approaches. First, the *steady-state models* by Ware et al. [50] and Mishra et al. [36] identify a steady state of the congestion-control dynamics, and predict BBR behavior with closed-form expressions for network metrics in this steady state. Second, the *dynamic fluid model* by Scherrer et al. [43] describes the transient behavior of BBR by means of ordinary differential equations (ODEs), and predicts BBR properties by fluid-model simulation, i.e., numerical ODE solving.

These two approaches suffer from a trade-off between accuracy and *interpretability*, i.e., transparency regarding the *causes* of model predictions. As we demonstrate in this work, the dynamic fluid model is more accurate than the steady-state models, mainly because the fluid-model can represent behavior outside the steady state. However, the dynamic fluid model has so far mostly been used for simulation, which arrives at predictions through lengthy numerical computation. As such, the predictions of dynamic fluid models are less explainable than the predictions of steady-state models, because steady-state models only consist of a handful of closed-form expressions that can be intuitively understood.

In this work, we aim to bridge this gap between accuracy and interpretability of model predictions. In particular, we demonstrate that a *control-theoretic analysis* of the dynamic fluid model allows insights

that are not only accurate and interpretable, but also rigorously provable. We illustrate the value of this stability analysis by focusing on the competition between BBR and CUBIC [18], the most prevalent CCAs in the Internet [35]. BBR/CUBIC competition frequently suffers from instability, i.e., *rate oscillation*, in which flows using different CCAs regularly obtain highly uneven bandwidth shares. While congestion-control oscillation (e.g., sawtooth in TCP Reno) is sometimes a necessary price to maximize utilization or achieve per-flow fairness, BBR/CUBIC oscillation is unnecessary and even harmful to fairness: Unfairness between BBR and CUBIC flows is especially pronounced when oscillation occurs (cf. §3.2).

Crucially, this instability is invisible in steady-state models, as these models assume stability. In contrast, fluid-model simulation reveals this oscillation, but must be conducted for specific network settings to indicate the occurrence and the severity of the oscillation. More general insights into the oscillation are possible thanks to our control-theoretic analysis of the fluid model: This analysis yields (i) mathematical conditions on network parameters, indicating when oscillation provably occurs, (ii) analytical bounds on the severity of the oscillation, describing the extreme rate distributions of BBR/CUBIC competition, and (iii) intuitive explanations of stabilizing adaptations of the BBR algorithm.

In summary, we present the following contributions:

Documentation of instability. We show that steady-state models predict BBR fairness towards CUBIC less accurately than dynamic models (§3.1), due to their assumption that BBR/CUBIC competition converges. In reality, convergence is prevented by persistent sending-rate oscillation, which we systematically explain for the first time (§3.2). While the oscillation is predicted accurately by fluid-model simulation, such simulation cannot provide a formal understanding of preconditions and severity of the oscillation.

Stability analysis of BBR/CUBIC fluid model. We apply a control-theoretic analysis to a joint BBR/CUBIC fluid model, thereby describing the BBR/CUBIC oscillation analytically and accurately. For this analysis, we first derive the equilibrium of the BBR/CUBIC fluid model (§4). Then, we derive an instability condition on network parameters, i.e., a network condition that is provably conducive to oscillation (§5). This condition is derived using Lyapunov theory, center-manifold theory, and fixed-point iteration.

Insights into temporal fairness. Besides identifying the preconditions for oscillation, the stability analysis also illuminates fairness implications of BBR/CUBIC oscillation, yielding worst-case fairness bounds and approximate tight fairness bounds that we experimentally validate (§6).

Countermeasure evaluation. We evaluate multiple adaptations of BBR regarding their effectiveness in suppressing oscillation, and explain the results by means of our control-theoretic framework (§7). These redesigned versions include several ad-hoc modifications of BBR, which we design and implement, and the official releases of BBRv2 and BBRv3. Importantly, these redesigns reduce oscillation, but still have drawbacks in terms of fairness or responsiveness.

This work does not raise any ethical issues.

2. Background

This section provides an overview of BBRv1 and CUBIC, the main CCAs in our analysis. BBRv2/v3 are discussed in §7.

2.1. BBRv1

Fundamentally, a BBRv1 flow maintains a *bottleneck-band-width estimate* x^{btl} and a *minimum-RTT estimate* $\tau^{\min}$. These two state variables determine the sending rate and are continuously adjusted by the following probing processes (Fig. 1).

Bandwidth probing. To regulate x^{btl}, a BBR flow cycles through periods of eight phases, where each phase lasts for the duration of the minimum-RTT estimate $\tau^{\min}$. In six of these phases, the pacing rate of the BBR flow is simply x^{btl}. However, in one phase (`ProbeBW_UP`), the BBR flow raises the pacing rate to $5/4 \cdot x^{\text{btl}}$ to discover whether more bandwidth is available. In the subsequent phase, the pacing rate is decreased to $3/4 \cdot x^{\text{btl}}$ to eliminate potential queues. The bottleneck-bandwidth estimate x^{btl} is continuously updated to the maximum measured delivery rate (ACK rate) from the last 10 RTTs.

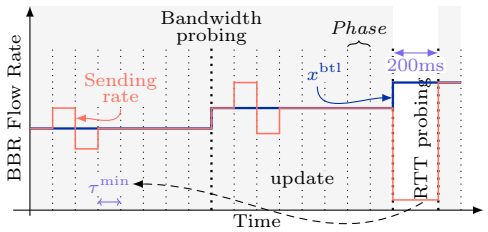

Figure 1: BBR.

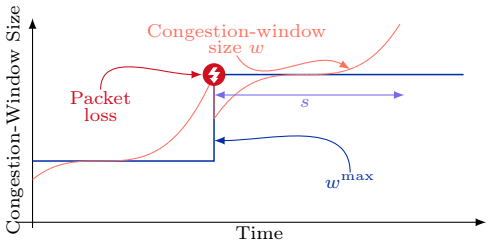

Figure 2: CUBIC.

RTT probing. Since the minimum-RTT estimate $\tau^{\min}$ should match the path propagation delay, $\tau^{\min}$ tracks the minimum measured RTT. If $\tau^{\min}$ cannot be adjusted for 10 seconds, BBR performs an *RTT-probing step*: Namely, the flow resets $\tau^{\min}$ and tries to drain the buffer by drastically reducing its sending rate for 200 milliseconds. This rate reduction is achieved by limiting the congestion window to 4 segments. At any other time, the BBR congestion-window size v amounts to twice the estimated BDP, i.e., $v = 2\tau^{\min}x^{\text{btl}}$. This congestion window may keep the sending rate below the pacing rate if the data volume 'in flight', i.e., sent but not acknowledged yet, grows due to congestion.

2.2. CUBIC

A CUBIC flow likewise maintains two state variables (Fig. 2), namely the *maximum congestion-window size* $w^{\max}$, which is recorded at the time of the last loss, and the *window-growth duration* s, which corresponds to the time since the last loss. These two variables determine the CUBIC congestion-window size w via the CUBIC window-growth function W:

$$w = W(w^{\max}, s) = w^{\max} + c \cdot \left(s - \sqrt[3]{\frac{b}{c} w^{\max}} \right)^3 . \tag{1}$$

In this function, the recommended parameters are $b = 0.3$ and $c = 0.4$ [42]. Hence, a packet loss ($s := 0$, $w^{>} := w$) instantly reduces the congestion-window size w by 30%.

3. Motivation

In this section, we show that dynamic models predict the outcome of BBR/CUBIC competition more accurately than steady-state models (§3.1). Steady-state models are less accurate in this regard because these models, while refreshingly simple, cannot represent transient phenomena (§3.2).

3.1. Comparison of Models

In previous research, the competition between BBR and CUBIC flows has been analyzed by means of steady-state models, namely by Ware et al. [50] and Mishra et al. [36]. These steady-state models have recently been complemented with a dynamic model by Scherrer et al. [43], who analyze BBR/CUBIC competition by means of fluid-model simulation, i.e., ODE solving. Fundamentally, steady-state models have no notion of time, but allow analytical investigation, whereas fluid-model simulations describe congestion-control behavior over time, but rely on numerical computation.

In this section, we evaluate all models with respect to their prediction accuracy for BBR/CUBIC competition. We describe our experiment setting in §3.1.1, and present our results in §3.1.2.

3.1.1. Experiment Setting

As usual in the literature [16, 19, 27, 38, 43, 44, 45, 50], we focus on a dumbbell topology with N senders sharing a single bottleneck link ℓ. This topology is pervasive in congestion-control studies as it captures the core challenge: achieving efficient and fair resource allocation among senders who lack direct communication and rely solely on network feedback to adjust their behavior. Additionally, its simplicity

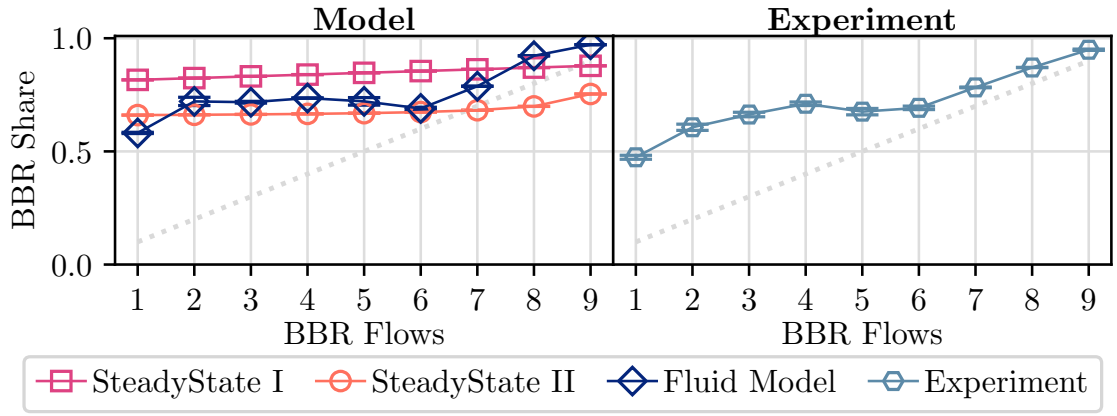

Figure 3: Model evaluation for 10 flows (The dotted gray line indicates the proportional share of BBR flows under perfect per-flow fairness).

makes it amenable to tractable theoretical analysis, enabling rigorous exploration of key dynamics. While this fundamental scenario can be extended to include more complex setups (e.g., multiple bottlenecks), the basic fan-in pattern of traffic remains highly relevant, particularly in real-world scenarios such as multiple users on a low-capacity residential edge link simultaneously downloading content from various sources.

In our experiments, the bottleneck link ℓ has capacity $C_\ell = 100$Mbps and a one-way propagation delay $\tau_\ell^{\mathrm{p}} = 10$ms. These link properties are in line with the capabilities of the network emulator Mininet [29] that we use. Each of the N senders accesses the bottleneck link ℓ via an individual non-shared link, also with a propagation delay of 10ms. Hence, the overall RTT propagation delay is $\tau^{\mathrm{p}} = 40$ms for each flow. The non-shared links and the bottleneck link are intermediated by a buffer with a size of 1.5 path BDP (750KB), as buffer sizes above 1 BDP are especially interesting for BBR/CUBIC fairness[1] [44, 50]. Each experiment lasts 120 seconds, and is repeated three times. All senders have infinite demand, generated by the *iperf* utility [34]. Unless otherwise stated, these settings are used for the remainder of the paper.

3.1.2. Results

We consider all BBR/CUBIC combinations in a network with $N = 10$ flows, and run all models plus the Mininet experiment for each combination. Then, we compute the obtained capacity share of all BBR flows. For the steady-state models, the capacity share is derived from the predicted steady-state rate distribution. For the fluid model and the experiments, the capacity share is the average capacity share over time. The results in Fig. 3 yield two important insights.

First, the BBR flows consistently obtain a disproportionately large capacity share, especially if they are in a minority. Hence, the fairness from the balanced scenario with 5 flows for each CCA is not generalizable.

Second and more importantly for our purpose, the predictive power of the models grows with their fidelity regarding the time dimension of the competition: The steady-state models (*SteadyState I* [50] and *SteadyState II* [36]) are less accurate than the fluid-model simulation (*Fluid Model*), which computes a time series for each network metric. This suggests that the steady-state perspective of BBR/CUBIC competition fails to capture important phenomena that unfold over time, i.e., the transient behavior of the competition.

3.2. The Relevance of Transient Behavior

The detailed results from the fluid-model simulations and the experiments (in Fig. 4) confirm that BBR/CUBIC competition involves transient phenomena, namely persistent *sending-rate oscillation*.

This oscillation is relevant for fairness, as the unfairness in Fig. 3 is particularly high whenever Fig. 4 indicates oscillation, i.e., for 1 to 5 BBR flows. In particular, the BBR flows obtain a egregiously over-proportional share of the bandwidth during the recurring peaks of the BBR rate oscillation.

[1] In smaller buffers, BBRv1 simply causes starvation of loss-based CCAs such as CUBIC [43].

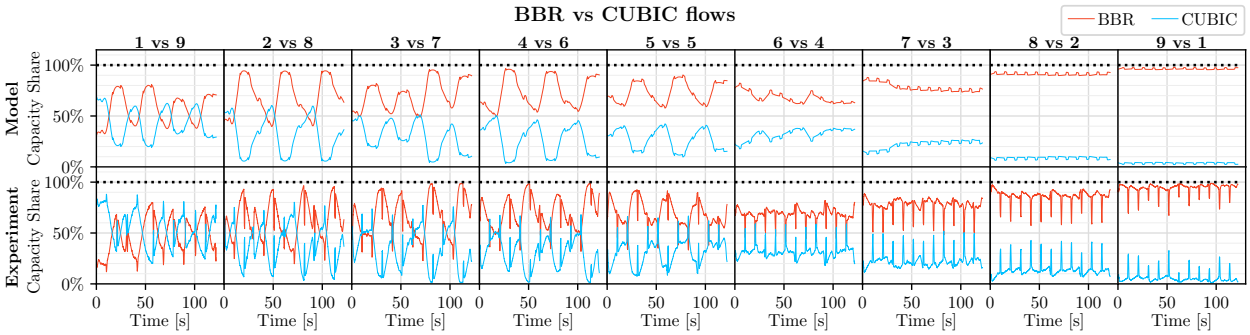

Figure 4: BBR/CUBIC competition over time for different CCA combinations (Aggregate capacity shares).

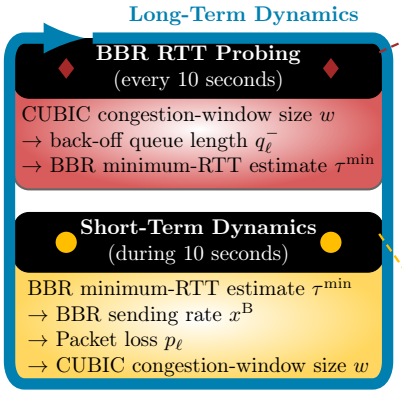

Figure 5: Basic mechanism of BBR/CUBIC oscillation.

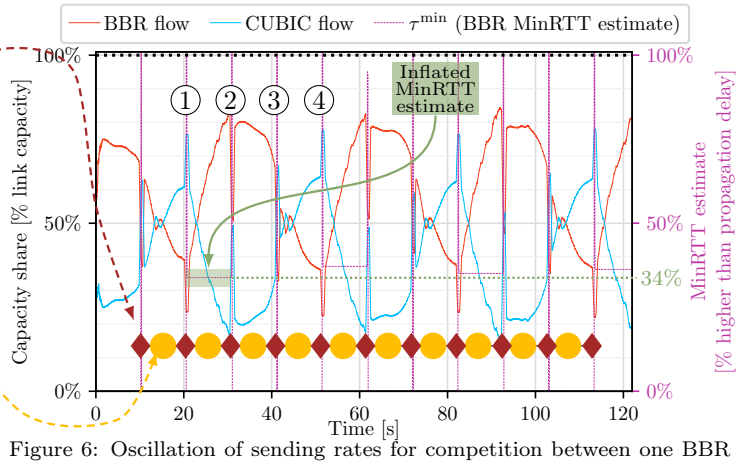

Figure 6: Oscillation of sending rates for competition between one BBR flow and one CUBIC flow (Experiment). The green line highlights an inflated MinRTT estimate by the BBR flow, leading to subsequent BBR rate growth.

While this oscillation has been noted in previous work [44], it has never been systematically explained. The following intuitive explanation helps understand the oscillation, but does not yet quantify its occurrence or severity; such quantitative results will be derived in Sections 4–6.

Oscillation in BBR/CUBIC competition is an alternation between (i) the *RTT probing step* of BBR, and (ii) the *short-term dynamics*, which are determined by the preceding RTT-probing step and last until the next RTT-probing step. This alternation forms the *long-term dynamics* (Figs. 5 and 6).

In the RTT-probing step, the BBR flow reduces its sending rate to almost zero, with the goal of emptying the buffer and discovering the propagation delay. However, the CUBIC flow does not participate in this reduction, and may thus prevent the complete clearance of the buffer if its congestion-window size w is relatively large at the time. The CUBIC congestion-window size w thus affects the *back-off queue length* q_ℓ^- during the RTT-probing step, and hence also the BBR minimum-RTT estimate $\tau^{\min}$ computed from probing measurements. For example, the CUBIC congestion-window size w in RTT-Probing Step ① in Fig. 6 is relatively large (cf. high CUBIC rate). As a result, the buffer is not completely cleared during RTT probing, and the minimum-RTT estimate $\tau^{\min}$ after the probing step (in interval [①,②] in Fig. 6) is around 34% higher than the actual propagation delay.

This inflated minimum-RTT estimate $\tau^{\min}$ co-determines the congestion-window size v of the BBR flow, and thus its sending rate x^{B}. Since this congestion-window size v actively constrains the BBR sending rate in scenarios with large buffers, the inflated minimum-RTT estimate also co-determines the BBR sending rate x^{B}. In particular, an inflated minimum-RTT estimate $\tau^{\min}$ (such as in time interval [①, ②] in Fig. 6) results in aggressive bandwidth probing by the BBR flow, which increases the BBR sending rate x^{B} and

reduces the CUBIC congestion-window size w by causing packet loss.

Crucially, this inflated $\tau^{\min}$ is fixed after RTT probing: Since the BBR flow and the CUBIC flow make intensive use of the buffer, they prevent a downward revision of the minimum-RTT estimate $\tau^{\min}$ during the short-term dynamics. Hence, these short-term dynamics continue until the minimum-RTT estimate $\tau^{\min}$ times out, i.e., for 10 seconds.

At the next RTT probing step, the reduced CUBIC congestion-window size w determines a new minimum-RTT estimate $\tau^{\min}$: For example, the reduced window size w at Step ② in Fig. 6 reduces the minimum-RTT estimate $\tau^{\min}$ to the propagation delay and thus induces a relatively low BBR rate x^{B}. Hence, the congestion-window size w increases again until Step ③. At Probing Step ③, w is still low enough to allow a correct estimate of the propagation delay and thus another growth phase of w. However, at Probing Step ④, $\tau^{\min}$ is inflated again and the oscillation pattern resumes.

This oscillation mechanism applies to the case with a single flow per CCA. However, oscillation may also arise for multiple flows per CCA, because simultaneous BBR flows synchronize their RTT-probing behavior (cf. Appendix A).

3.3. Conclusion

In summary, the fairness of BBR/CUBIC competition is heavily determined by the transient phenomenon of oscillation. This oscillation is fundamentally impossible to predict for the time-agnostic steady-state models, but is predicted with high accuracy by fluid-model simulations.

However, these simulations must be computed for a specific network setting of interest, and therefore do not allow fundamental insights to the same degree as analytical investigations would. In particular, the numerical simulations do not constitute rigorous proofs, e.g., regarding the conditions under which oscillation provably occurs, or regarding worst-case bounds for the unfairness of BBR/CUBIC competition.

In this paper, we therefore apply control theory to the dynamic fluid model. This control-theoretic analysis relies on the equilibrium of the dynamic fluid model (§4), which is then leveraged for an analysis of oscillation conditions (§5), oscillation bounds (§6), and oscillation suppression (§7).

4. Fluid-Model Equilibrium

To enable control-theoretic analysis, we construct a joint fluid model of BBR/CUBIC competition by combining our BBR model from previous work [43] with the CUBIC model of Vardoyan et al. [48]. The resulting system is governed by the differential equations Eqs. (DE1)–(DE3). From this formulation, we derive the corresponding equilibrium, which serves as the foundation for our control-theoretic analysis. Our approach remains consistent with prior work, but extends these models by providing an integrated framework that supports explanatory reasoning and yields additional predictions beyond those available from the original formulations.

Relevance. The fluid-model equilibrium is crucial for analyzing the convergence of BBR and CUBIC flows, as the fluid-model equilibrium is a fixed point of the large-scale BBR/CUBIC dynamics: Once the competing flows adopt the rate distribution in the fluid-model equilibrium, they maintain this rate distribution for the entire future of their competition, apart from small-scale fluctuations inherent in the congestion-control algorithms (e.g., the 5/4-3/4 pacing-rate variation in BBR). Therefore, if the BBR/CUBIC dynamics arrived at this equilibrium, the observed large-scale oscillation would not occur; however, it is a separate question whether the BBR/CUBIC dynamics arrive at this fixed point from a non-equilibrium initial configuration. This question will be investigated in the next section (§5).

4.1. Fluid-Model Basics

We consider N_{B} BBR flows in set F_{B} and N_{C} CUBIC flows in set F_{C}, all of which share a single bottleneck link ℓ. According to Scherrer et al. [43], each BBR flow i generally sends at rate $x_i^{\mathrm{B}} = \beta_i x_i^{\mathrm{btl}}$, where x_i^{btl} is the bottleneck-bandwidth estimate of flow i, and β_i is the flow's *strength*. This strength coefficient β_i

BBR	α	Probing strength (Rate coefficient under active bandwidth probing)
	β	Strength (Rate coefficient under inactive bandwidth probing)
	$\tau^{\min}$	Minimum-RTT estimate
	$v = 2x^{\mathrm{btl}}\tau^{\min}$	Congestion-window size
	x^{B}	BBR sending rate
	x^{btl}	Bottleneck-bandwidth estimate
	x^{dlv}	Measured delivery rate
	$\chi > 0$	Minimum bottleneck-bandwidth estimate
CUBIC	$b = 0.3$	Loss-reduction parameter
	$c = 0.4$	Window-scaling parameter
	s	Window-growth duration
	w	Congestion-window size
	$w^{\max}$	Maximum congestion-window size
	$W(w^{\max}, s)$	Window-growth function
	x^{C}	CUBIC sending rate
Network	p_ℓ	Loss rate on link ℓ
	q_ℓ	Queue length of link ℓ
	q_ℓ^-	Back-off queue length of link ℓ (during BBR RTT probing)
	y_ℓ	Total sending rate on link ℓ
	τ_f	Total delay (RTT) experienced by flow f
	τ_f^{p}	Propagation delay on path used by flow f
Stability analysis	$\sigma = (x^{\mathrm{btl}}, w^{\max}, s)$	System state (Irreducible state variables)
	$\tilde{\cdot}$	Value of state variable in *short-term* equilibrium
	$\bar{\cdot}$	Value of state variable in *long-term* equilibrium
	$w^{\leftarrow}(w)$	Window-update function under *incomplete* convergence (CUBIC congestion-window size at an RTT-probing step after a previous RTT-probing step where the CUBIC congestion-window size was w)
	$\tilde{w}^{\leftarrow}(w)$	Window-update function under *complete* convergence (Short-term equilibrium CUBIC congestion-window size after an RTT-probing step where the CUBIC congestion-window size was w)
	$w^{<}$	Minimum possible CUBIC congestion-window size in equilibrium
	$w^{>}$	Maximum possible CUBIC congestion-window size in equilibrium
	Ω	Unstable neighborhood of long-term equilibrium CUBIC window size $\overline{w}$

Table 1: Notation used in formal analysis

enforces the congestion-window constraint on the BBR sending rate. The BBR congestion-window size is $v_i = 2\tau_i^{\min} x^{\mathrm{btl}}$, where $\tau_i^{\min}$ is the minimum-RTT estimate of BBR flow i.

$$\beta_i = \min\left(1, 2\tau_i^{\min}/\tau_i\right), \tag{2}$$

where τ_i is the current delay experienced by BBR flow i.

In contrast, each CUBIC flow k sends at rate $x_k^{\mathrm{C}} = w_k/\tau_k$, where w_k is the current congestion window

of CUBIC flow k and τ_k is the currently experienced delay of flow k. The congestion-window size w_k is determined by the CUBIC window-growth function $W(w^{\max}, s)$ in Eq. (1).

The total load y_ℓ on link ℓ is thus given by:

$$y_\ell = \sum_{i \in F_\mathrm{B}} x_i^\mathrm{B} + \sum_{k \in F_\mathrm{C}} x_i^\mathrm{C} = \sum_{i \in F_\mathrm{B}} \beta_i x_i^\mathrm{btl} + \sum_{k \in F_\mathrm{C}} \frac{w_k}{\tau_k}. \tag{3}$$

Note that this formulation of y_ℓ is an approximation by Scherrer et al. [43], as the BBR flows deviate from the rate $\beta_i x^\mathrm{btl}$ when they are probing for bandwidth (cf. §2.1), i.e., when they increase the rate to $5/4 \cdot x^\mathrm{btl}$ in one bandwidth-probing phase and reduce it to $3/4 \cdot x^\mathrm{btl}$ in the next phase. However, these bandwidth-probing deviations happen in only two consecutive phases of the 8-phase bandwidth-probing cycle, and tend to cancel each other when averaged over time. Hence, we adopt Eq. (3) as a suitable approximation for the large-scale link-load dynamics that are relevant for the fluid-model equilibrium.

The loss rate p_ℓ is based on the *excess* sending rate:

$$p_\ell = \begin{cases} \frac{y_\ell - C_\ell}{y_\ell} & \text{if } y_\ell > C_\ell \wedge q_\ell = B_\ell, \\ 0 & \text{otherwise,} \end{cases} \tag{4}$$

where C_ℓ, q_ℓ, and B_ℓ are the link capacity, queue length and buffer size at the bottleneck link ℓ, respectively.

4.2. CUBIC Equilibrium

The behavior of a CUBIC flow k is captured by the two variables $w_k^{\max}$ and s_k, which evolve as follows in the model by Vardoyan et al. [48]:

$$\dot{w}_k^{\max} = (w_k - w_k^{\max}) \cdot x_k^\mathrm{C} \cdot p_\ell \tag{DE1}$$

$$\dot{s}_k = 1 - s_k \cdot x_k^\mathrm{C} \cdot p_\ell \tag{DE2}$$

Eq. (DE1) adjusts the maximum recorded window $w^{\max}$ towards the current window for each lost segment. Similarly, Eq. (DE2) resets the window-growth duration s to 0 for each lost segment, and lets s grow linearly in absence of loss.

Given these CUBIC dynamics, we are now interested in the *fluid equilibrium* of CUBIC flows, i.e., the values $\overline{w}_k^{\max}$ and $\overline{s}_k$ that are preserved by the dynamics in Eqs. (DE1) and (DE2). This complete stasis is possible in fluid models because fluid models approximate network metrics in a time-averaged manner; in reality, network metrics fluctuate around their fluid average and never become fully static. In the fluid model, the CUBIC state variables are in equilibrium if

$$\forall k \in F_\mathrm{C}. \qquad \dot{w}_k^{\max} = (\overline{w}_k - \overline{w}_k^{\max}) \cdot \overline{x}_k^\mathrm{C} \cdot \overline{p}_\ell = 0 \tag{5}$$

$$\dot{s}_k = 1 - \overline{s}_k \cdot \overline{x}_k^\mathrm{C} \cdot \overline{p}_\ell = 0 \tag{6}$$

Eq. (6) implies that none of $\overline{s}_k$, $\overline{x}_k^\mathrm{C}$, and $\overline{p}_\ell$ can be zero in equilibrium. We apply this insight on Eq. (5):

$$\begin{aligned} &\dot{w}_k^{\max} = 0 \underset{\overline{x}_k^\mathrm{C}, \overline{p}_\ell \neq 0}{\overset{\text{Eq. (5)}}{\iff}} \overline{w}_k = \overline{w}_k^{\max} \overset{\text{Eq. (1)}}{\iff} \\ &\overline{w}_k^{\max} = \overline{w}_k^{\max} + c \left(\overline{s}_k - \sqrt[3]{\frac{\overline{w}_k^{\max} b}{c}} \right)^3 \overset{\text{solve}}{\iff} \overline{w}_k^{\max} = \frac{c}{b} \overline{s}_k^3. \end{aligned} \tag{7}$$

Hence, in the fluid equilibrium, the congestion-window size w_k is constant over time. This stasis is enabled by the *CUBIC-stabilizing loss* $\overline{p}_\ell$, which balances growth and reduction in the fluid-averaged congestion-window size w_k (In reality, the CUBIC window size will fluctuate in presence of loss). This loss $\overline{p}_\ell$ is obtained by inserting $\overline{x}_k^\mathrm{C} = \overline{w}_k^{\max} / \overline{\tau}_k$ into Eq. (6):

$$\dot{s}_k \overset{(6)}{=} 1 - \overline{s}_k \cdot \overline{x}_k^\mathrm{C} \cdot \overline{p}_\ell = 0 \overset{\text{Eq. (7)}}{\iff} \overline{p}_\ell = \frac{b \overline{\tau}_k}{c \overline{s}_k^4} > 0. \tag{8}$$

This CUBIC-stabilizing loss $\overline{p}_\ell$ must correspond to the actually occurring loss from Eq. (4), which in turn depends on the sending rates of *both* CUBIC and BBR flows:

Lemma 1. ***CUBIC Equilibrium Conditions:***

$$\forall k \in F_{\mathrm{C}}. \quad \overline{p}_\ell = \frac{b\overline{\tau}_k}{c\overline{s}_k^4} = \frac{\overline{y}_\ell - C_\ell}{\overline{y}_\ell} \tag{9}$$

Since $\overline{s}_k > 0$ follows from Eq. (6), Eq. (8) implies $\overline{p}_\ell > 0$, i.e., the equilibrium requires that congestion fills the whole buffer ($\overline{q}_\ell = B_\ell$) and loss occurs. For that reason, the delays in the fluid equilibrium become:

$$\forall j \in F_{\mathrm{B}} \cup F_{\mathrm{C}}. \quad \overline{\tau}_j = \tau_j^{\mathrm{p}} + \frac{\overline{q}_\ell}{C_\ell} = \tau_j^{\mathrm{p}} + \frac{B_\ell}{C_\ell}, \tag{10}$$

where τ_j^{p} is the propagation delay experienced by flow j.

4.3. BBR Equilibrium

The bottleneck estimate x_i^{btl} of BBR flow i tracks the maximum delivery rate x_i^{dlv} [43], reflected in a differential equation that continuously adjusts x_i^{btl} towards x_i^{dlv}:

$$\dot{x}_i^{\mathrm{btl}} = x_i^{\mathrm{dlv}} - x_i^{\mathrm{btl}} \tag{DE3}$$

with

$$x_i^{\mathrm{dlv}} = \begin{cases} \frac{\alpha_i x_i^{\mathrm{btl}} C_\ell}{y_\ell + (\alpha_i - \beta_i) x_i^{\mathrm{btl}}} & \text{if } y_\ell + (\alpha_i - \beta_i) x_i^{\mathrm{btl}} \geq C_\ell, \\ \alpha_i x_i^{\mathrm{btl}} & \text{otherwise,} \end{cases} \tag{11}$$

where α_i denotes the *probing strength* of the BBR flow: In its 8-RTT bandwidth-probing cycle, a BBR flow raises its pacing rate during a single RTT (`ProbeBW_UP` phase) to discover whether additional bandwidth is available. In this phase, the BBR flow sets the pacing rate to $5/4 \cdot x_i^{\mathrm{btl}}$, while being constrained by the congestion-window size of $2\tau_i^{\min} x^{\mathrm{btl}}$:

$$\alpha_i = \min\left(5/4,\ 2\tau_i^{\min}/\tau_i\right). \tag{12}$$

We now extend previous work by identifying the BBR/ CUBIC equilibrium (outside of the RTT-probing steps). Since $\overline{y}_\ell > C_\ell$ (implied by Lemma 1) and $\alpha_i \geq \beta_i$ (Eqs. (2) and (12)), Eq. (DE3) implies the BBR equilibrium condition:

$$\forall i \in F_{\mathrm{B}}. \quad \frac{\overline{\alpha}_i \overline{x}_i^{\mathrm{btl}} C_\ell}{\overline{y}_\ell + \left(\overline{\alpha}_i - \overline{\beta}_i\right) \overline{x}_i^{\mathrm{btl}}} - \overline{x}_i^{\mathrm{btl}} = 0. \tag{13}$$

These conditions admit the equilibrium $\overline{x}_i^{\mathrm{btl}} = 0\ \forall i$. However, $\overline{x}_i^{\mathrm{btl}} = 0$ is an artificial equilibrium: The BBR implementation never sets x^{btl} to zero, even under 100% packet loss, to allow recovery of the sending rate [22]. Effectively, x^{btl} is thus lower-bounded by some small number $\chi > 0$. Hence, we arrive at the following equilibrium conditions:

Lemma 2. ***BBR Equilibrium Conditions:*** $\forall i \in F_{\mathrm{B}}$.

$$\overline{x}_i^{\mathrm{btl}} = \max\left(\chi,\ C_\ell - \frac{1}{\overline{\alpha}_i}\left(\sum_{j \in F_{\mathrm{B}} \setminus \{i\}} \overline{\beta}_j \overline{x}_j^{\mathrm{btl}} + \sum_{k \in F_{\mathrm{C}}} \overline{x}_k^{\mathrm{C}}\right)\right) \tag{14}$$

To determine the strengths $\overline{\alpha}_i$ and $\overline{\beta}_i$ in equilibrium, we first note that the CUBIC equilibrium conditions in Lemma 1 imply a consistently full buffer in equilibrium (outside the RTT-probing steps). Hence, the BBR flows never spontaneously observe decreasing RTT samples in equilibrium, and must perform an RTT-probing step every 10 seconds. In an RTT-probing step, a BBR flow i reduces its congestion window to 4 segments, with the goal of uncovering the path propagation delay τ_i^{p}. Intriguingly, BBR flows synchronize their RTT-probing steps (cf. Appendix A) such that the propagation delay is indeed uncovered if only BBR

flows compete. However, in our scenario, the bottleneck link ℓ is shared with CUBIC flows, which do not participate in the buffer draining. Hence, the equilibrium min-RTT estimate $\overline{\tau}_i^{\min}$ is inflated by the minimal *back-off queue length* $\overline{q}_\ell^-$ remaining in the RTT-probing step:

$$\overline{q}_\ell^- = \left[4N_{\mathrm{B}} + (1-b)\sum_{k\in F_{\mathrm{C}}} \overline{w}_k - \tau_\ell^{\mathrm{p}} C_\ell\right]_0^{B_\ell} \implies \overline{\tau}_i^{\min} = \tau_i^{\mathrm{p}} + \frac{\overline{q}_\ell^-}{C_\ell}. \tag{15}$$

Since $\overline{q}_\ell^-$ can neither be negative nor exceed the bottleneck-buffer capacity B_ℓ, we use the notation $[\cdot]_0^{B_\ell}$ for projection to the interval $[0, B_\ell]$. Intuitively, the remaining queue volume $\overline{q}_\ell^-$ contains the inflight volume of all flows when the BBR flows are in an RTT-probing step and the CUBIC flows are minimal, i.e., back off because of loss (factor $1-b$). In case of congestion, this inflight data tends to accumulate on the bottleneck link ℓ. Hence, this inflight data is discounted by the volume that fits in the pipe, i.e., the BDP $\tau_\ell^{\mathrm{p}} C_\ell$ (τ_ℓ^{p} being the propagation delay of bottleneck link ℓ).

The equilibrium conditions in Lemma 1 (CUBIC flows) and in Lemma 2 (BBR flows) form a system of $N = N_{\mathrm{B}} + N_{\mathrm{C}}$ nonlinear equations with N variables. This equation system can then be solved to compute an equilibrium rate distribution. While such solutions are difficult in general, the starvation of BBR flow i is easy to derive given $\overline{\alpha}_i \leq 1$:

Lemma 3. ***Sufficient Condition for BBR Starvation:***

$$\overline{\alpha}_i \leq 1 \quad \implies \quad \overline{x}_i^{\mathrm{btl}} = \chi \tag{16}$$

Proof. From Lemma 1, we know that $\overline{y}_\ell > C_\ell$, and hence:

$$\begin{aligned} \overline{y}_\ell > C_\ell \overset{\overline{\alpha}_i \leq 1}{\iff} \overline{y}_\ell > \overline{\alpha}_i C_\ell \overset{/\overline{y}_\ell}{\underset{-1}{\iff}} 0 > \frac{\overline{\alpha}_i C_\ell}{\overline{y}_\ell} - 1 \\ \overset{\dot{\overline{x}}_i^{\mathrm{btl}}}{\underset{\overline{\alpha}_i = \overline{\beta}_i}{\iff}} 0 > \frac{\overline{\alpha}_i \overline{x}_i^{\mathrm{btl}} C_\ell}{\overline{y}_\ell + (\overline{\alpha}_i - \overline{\beta}_i)\overline{x}_i^{\mathrm{btl}}} - \overline{x}_i^{\mathrm{btl}} = \dot{\overline{x}}_i^{\mathrm{btl}} \end{aligned} \tag{17}$$

Therefore, if $x_i^{\mathrm{btl}} = \chi$, BBR would reduce x_i^{btl} further, but cannot. Hence, $\overline{x}_i^{\mathrm{btl}} = \chi$ is the unique equilibrium. □

5. Conditions for Oscillation

In this section, we derive analytical conditions under which BBR/CUBIC oscillation provably occurs.

5.1. Analysis Overview

We distinguish short-term and long-term dynamics (Fig. 5).

The *short-term dynamics* describe the continuous BBR/CUBIC competition *between* the RTT probing steps of BBR. Between these probing steps, the BBR probing strength α is fixed, and fully determines the equilibria (§5.2) and the convergence behavior (§5.3) of the short-term dynamics.

Building on these short-term dynamics, we derive the *long-term dynamics*, describing the BBR/CUBIC competition *across* RTT-probing steps (§5.4). In each RTT-probing step, the CUBIC congestion-window size w determines the probing strength α (Eq. (12)) and thus the short-term dynamics for the next 10 seconds. These short-term dynamics then determine the congestion-window size w at the next RTT-probing step. Hence, the long-term dynamics form a discrete process.

In the following, we consider the case for one BBR flow and one CUBIC flow ($N_{\mathrm{B}} = 1$, $N_{\mathrm{C}} = 1$). For simplicity, we thus eliminate the flow-specific subscripts i and k where the association is obvious, e.g., only the BBR flow i has a probing strength $\alpha_i = \alpha$. As discussed in Appendix A, the scenarios for multiple flows per CCA are qualitatively similar for a majority of CCA compositions.

5.2. Short-Term Equilibria

In §3.2, we observed that the minimum-RTT estimate $\tau^{\min}$ of the BBR flow i is only periodically updated in competition with CUBIC. To investigate the dynamics between these updates, we can thus treat $\tau^{\min}$ as fixed, and by extension also the probing strength α (cf. Eq. (12)). This fixed α then determines the equilibrium $\tilde{\sigma}(\alpha)$ of the short-term dynamics:

Theorem 1. ***Unique Short-Term Equilibrium.*** *Given probing strength α, the unique short-term equilibrium $\tilde{\sigma}(\alpha) = (\tilde{x}^{\mathrm{btl}}(\alpha), \tilde{w}^{\max}(\alpha), \tilde{s}(\alpha))$ for competition between BBR flow i and CUBIC flow k on a bottleneck link ℓ can be computed as follows:*

1. *Find discriminant probing strength $\hat{\alpha}$ for the considered network by solving:*

$$\frac{\hat{\alpha}^4(\hat{\alpha}-1)^3}{(\chi+\hat{\alpha}(C_\ell-\chi))^3} = \frac{c}{b\overline{\tau}_k(C_\ell-\chi)^7}, \tag{18}$$

2. *Find equilibrium CUBIC window-growth duration $\tilde{s}(\alpha)$ by solving:*

$$\boldsymbol{\alpha \geq \hat{\alpha}:} \qquad \tilde{S}_1(\tilde{s}) = \frac{(\alpha-1)c^2}{\alpha b\overline{\tau}_k}\tilde{s}^7 - \frac{(\alpha-1)\,c}{\alpha}\tilde{s}^3 - bC_\ell\overline{\tau}_k = 0 \tag{19}$$

$$\boldsymbol{\alpha < \hat{\alpha}:} \qquad \tilde{S}_2(\tilde{s}) = \frac{c^2}{b\overline{\tau}_k}\tilde{s}^7 - c\,(C_\ell-\alpha\chi)\,\tilde{s}^4 - c\tilde{s}^3 - \alpha b\overline{\tau}_k\chi = 0, \tag{20}$$

3. *Compute equilibrium CUBIC congestion window size $\tilde{w}^{\max}(\alpha) = \frac{c}{b}\tilde{s}(\alpha)^3$*

4. *Compute equilibrium BBR bottleneck estimate* $\tilde{x}^{\mathrm{btl}}(\alpha) = \begin{cases} C_\ell - \frac{\tilde{w}^{\max}(\alpha)}{\alpha\overline{\tau}_k} & \text{if } \alpha \geq \hat{\alpha}, \\ \chi & \text{if } \alpha < \hat{\alpha} \end{cases}$

Proof Sketch. The full proof of Theorem 1 is provided in §Appendix B. The proof first considers the case $\alpha \leq 1$, which implies $\tilde{x}^{\mathrm{btl}}(\alpha) = \chi$ according to Lemma 3. Inserting this value into the CUBIC equilibrium conditions from Lemma 1 yields the condition $\tilde{S}_2(s) = 0$. The septic polynomial $\tilde{S}_2$ has a unique root, which guarantees a unique equilibrium $\tilde{s}(\alpha)$. Second, the proof considers the case $\alpha > 1$, and distinguishes the sub-cases $\hat{x}^{\mathrm{btl}} \geq \chi$ and $\hat{x}^{\mathrm{btl}} < \chi$, where $\hat{x}^{\mathrm{btl}} = C_\ell - \tilde{x}^{\mathrm{C}}/\alpha$ is the equilibrium BBR bottleneck-bandwidth estimate without restriction to the domain $[\chi, \infty)$. If $\hat{x}^{\mathrm{btl}} \geq \chi$, combining $\tilde{x}^{\mathrm{btl}} = \hat{x}^{\mathrm{btl}}$ with the CUBIC equilibrium conditions from Lemma 2 yields $\tilde{S}_1(s) = 0$, which again has a unique solution. For the other sub-case $\hat{x}^{\mathrm{btl}} < \chi$, we identify the probing strength $\hat{\alpha} > 1$ (with Eq. (18)) such that χ is an unrestricted equilibrium, i.e., $\hat{x}^{\mathrm{btl}} = \tilde{x}^{\mathrm{btl}} = \chi$. For any $\alpha < \hat{\alpha}$, it holds that $\hat{x}^{\mathrm{btl}} < \chi$ and thus $\tilde{x}^{\mathrm{btl}}(\alpha) = \chi$. □

5.3. Stability of Short-Term Equilibria

For the short-term equilibria to be relevant, the short-term dynamics have to converge to these equilibria. This attractiveness is necessary for the BBR/CUBIC dynamics to converge to a new short-term equilibrium rate distribution if the minimum-RTT estimate $\tau^{\min}$ is updated and α thus changes. To confirm the attractiveness of the short-term equilibria, we prove the *asymptotic stability* of these equilibria, meaning that the competition converges to the short-term equilibrium if the initial rate distribution is close enough:

Theorem 2. ***Stability of Short-Term Equilibrium.*** *In the competition between one BBR flow and one CUBIC flow, the short-term equilibrium $\tilde{\sigma}(\alpha) = (\tilde{x}^{\mathrm{btl}}(\alpha),\ \tilde{w}^{\max}(\alpha),\ \tilde{s}(\alpha))$ of the joint dynamics is asymptotically stable, i.e., the BBR/CUBIC dynamics converge to the rate distribution of equilibrium $\tilde{\sigma}(\alpha)$.*

Proof Sketch. We provide the full rigorous proof in §Appendix C, and provide a high-level overview here.

Importantly, a straightforward stability proof via linearization of the dynamic system fails, for the reasons already noted by Vardoyan et al. [48] who considered a CUBIC flow in isolation. Namely, when the

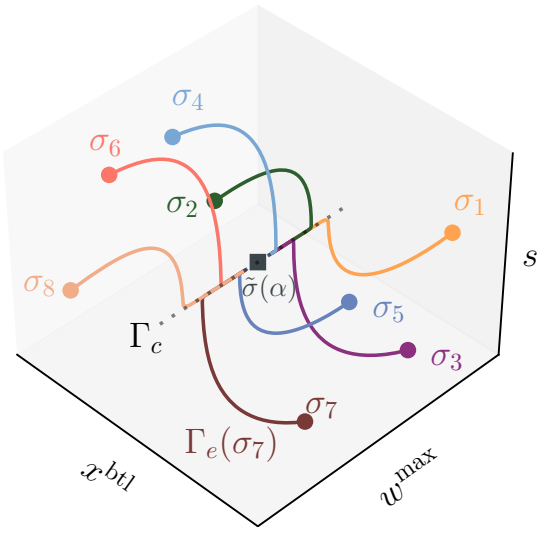

Figure 7: Two-step convergence in short-term dynamics: First exponential convergence *towards* the center manifold Γ_c (a function of $w^{\max}$), then sub-exponential *along* Γ_c towards the short-term equilibrium $\tilde{\sigma}(\alpha)$.

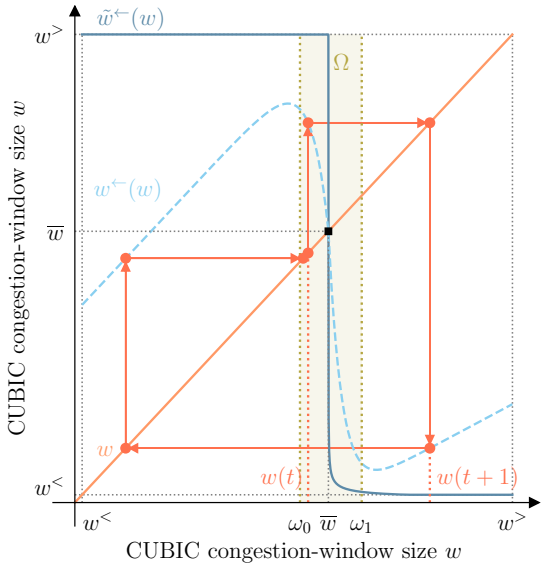

Figure 8: Instability of long-term dynamics: Under the condition from Theorem 3, the dynamics suffer from persistent oscillation as the evolution trajectory moves away from the CUBIC long-term equilibrium window $\overline{w}$.

BBR/CUBIC dynamics approach the equilibrium $\tilde{\sigma}(\alpha)$, the evolution of the CUBIC maximum window $w^{\max}$ is exclusively determined by high-order terms that are not captured by the linearization. Formally, the Jacobian matrix of the BBR/CUBIC differential-equation system has both zero and negative eigenvalues when evaluated at equilibrium, rendering the stability investigation via linearization inconclusive. Hence, more advanced methods are required.

In our case, we can rely on the *center-manifold emergence theorem* [21]: Given inconclusive linearization, the dynamics converge exponentially fast to the *center manifold* and then approximately follow a slow (i.e., sub-exponential) trajectory along the center manifold. The center manifold contains the equilibrium, so the behavior of trajectories on this manifold determines convergence to equilibrium. Moreover, because the center manifold is typically low-dimensional, it allows a tractable analysis of the system's stability.

More precisely, the differential-equation system is first transformed into the eigenbasis of the linearized system (i.e., of the Jacobian matrix), which decouples the state into center and stable subspaces; the center variable corresponds to the direction with zero eigenvalue (the center subspace), while the stable variables correspond to directions with negative eigenvalues (the stable subspace). Expressing the stable variables as functions of the center variable, the dynamics are then projected onto the center manifold, giving a one-dimensional equation that governs motion along the center manifold. Stability can then be analyzed directly in this reduced one-dimensional system.

Figure 7 illustrates this convergence behavior for the dynamics between one BBR flow and one CUBIC flow. As these dynamics involve the three variables x^{btl} (for the BBR flow), $w^{\max}$, and s (both for the CUBIC flow), the state space of the competition dynamics is three-dimensional. The system evolution from a starting point σ_n is a path through the state space. This path is determined by the differential equations governing the three variables, and is visualized by a curve $\Gamma_e(\sigma_n)$ in the three-dimensional space. This evolution curve $\Gamma_e(\sigma_n)$ approaches the center manifold exponentially quickly. In our proof, this center manifold can be expressed by means of the single variable $w^{\max}$, and thus corresponds to another curve Γ_c. Moreover, the system-evolution path $\Gamma_e(\sigma_n)$ tracks the center-manifold curve Γ_c towards the equilibrium $\tilde{\sigma}(\alpha)$, illustrating that the short-term equilibrium is asymptotically stable. □

5.4. Long-Term Dynamics

So far, our analysis suggests that the BBR/CUBIC dynamics converge to a short-term equilibrium $\tilde{\sigma}(\alpha)$ for a fixed minimum-RTT estimate $\tau^{\min}$ and fixed probing strength α. While $\tau^{\min}$ is indeed fixed for periods of time, it is also regularly adjusted, at least every 10 seconds: To readjust $\tau^{\min}$, the BBR flow measures the RTT during RTT probing, meaning the RTT determined by the back-off queue length q_ℓ^- from Eq. (15). In turn, this back-off queue length is determined by the CUBIC congestion-window size w at the time of RTT probing, because part of that CUBIC volume resides in the buffer.

During RTT probing, the CUBIC congestion-window size w is evolving towards the window size $\tilde{w}(\alpha') = \tilde{w}^{\max}(\alpha')$ as defined in Eq. (7)). This target equilibrium depends on the previous probing strength α'.

However, convergence is typically incomplete by the time RTT probing occurs. The reason is that the state variable $w^{\max}$, which governs the evolution of the CUBIC window, approaches its equilibrium only with sub-exponential speed (see Theorem 1). As a consequence, the actual window size at probing, denoted by w', may differ from the short-term equilibrium, i.e., $w' \neq \tilde{w}(\alpha')$. This intermediate size w' is then used to readjust the probing strength α.

Thus, the long-term evolution of the CUBIC window size w is described by the discrete-time process:

$$\forall t \in \mathbb{N}, t \geq 0. \quad w(t+1) = w^{\leftarrow}(w(t)). \tag{21}$$

Here, t indexes the probing steps of BBR, which are separated by about 10 seconds. The function $w^{\leftarrow}$ maps the starting window size $w(t)$ to the resulting window size after one probing interval. This function $w^{\leftarrow}$ reflects the short-term dynamics between t and $t+1$. These short-term dynamics are governed by the probing strength α during the interval, which is itself determined by the window size $w(t)$ at the beginning of the interval. Within a probing interval, the BBR bandwidth estimate x^{btl} converges much faster than the CUBIC window (see Theorem 1). Consequently, the initial value $x^{\mathrm{btl}}(t)$ has negligible influence on $w^{\leftarrow}$.

Hence, we distinguish between two update functions:

- **Idealized update function** $\tilde{w}^{\leftarrow}(w)$: assumes complete short-term convergence within an interval, producing the short-term equilibrium window size $\tilde{w}$, and
- **Actual update function** $w^{\leftarrow}(w)$: may stop short of equilibrium and is therefore only bounded between w and $\tilde{w}^{\leftarrow}(w)$.

The process in (21) is guaranteed to have a unique long-term equilibrium window size $\overline{w}$, corresponding to the fluid-model equilibrium from §4. However, under mild conditions, this equilibrium is *unstable*:

Theorem 3. ***Instability of Long-Term Equilibrium.*** *Consider the dynamics of a BBR flow competing with a CUBIC flow. There exists a unique long-term CUBIC equilibrium window size $\overline{w}$, defined by the fixed point of $w^{\leftarrow}$. This equilibrium is unstable, meaning that trajectories do not converge to $\overline{w}$ even when starting arbitrarily close, if there exists a neighborhood Ω in which the window-update function $w^{\leftarrow}(w)$ decreases fast enough in w:*

$$\exists\ \Omega = [\omega_0, \omega_1],\ \omega_0 < \overline{w} < \omega_1. \quad \forall \omega \in \Omega. \quad \frac{\partial w^{\leftarrow}(\omega)}{\partial \omega} < -1 \tag{22}$$

Proof Sketch. The proof from §Appendix D can be visualized using the fixed-point diagram in Fig. 8.

First, consider the idealized update function $\tilde{w}^{\leftarrow}(w)$. The function $\tilde{w}^{\leftarrow}$ is fully known, bounded to the finite range $[w^{<}, w^{>}]$ (derived in §Appendix D), and monotonic. Thus, $\tilde{w}^{\leftarrow}$ intersects the identity line exactly once, at $\overline{w}$, which is thus a unique long-term equilibrium window size $\overline{w}$.

In contrast, the actual update function $w^{\leftarrow}(w)$ is not known in closed form. However, we can state that for any starting window size w, the resulting value $w^{\leftarrow}(w)$ lies between w and $\tilde{w}^{\leftarrow}(w)$. This property follows from the asymptotic stability of the short-term equilibrium (see Theorem 2): the CUBIC window tends toward $\tilde{w}$ while α is fixed, but convergence may be incomplete when α is updated.

We can now describe the discrete-time evolution: Starting from a point $(w(t), w(t))$ on the identity line, the update step projects vertically to $(w(t), w^{\leftarrow}(w(t)))$ on the curve of $w^{\leftarrow}$. We then obtain the next state $w(t+1)$ by projecting horizontally to the identity line. Repeating this procedure yields the system trajectory.

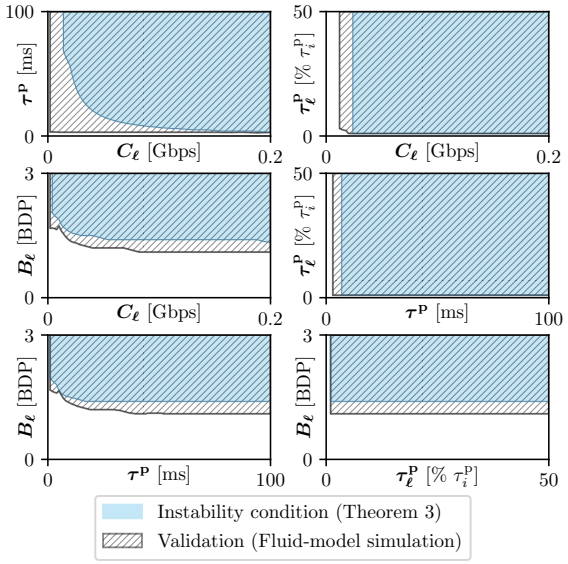

Figure 9: Network-parameter space (blue) that satisfies the oscillation condition from Theorem 3. The shaded area marks the parameter space for which the fluid-model simulation indicates oscillation (Constant parameters listed in §5.5).

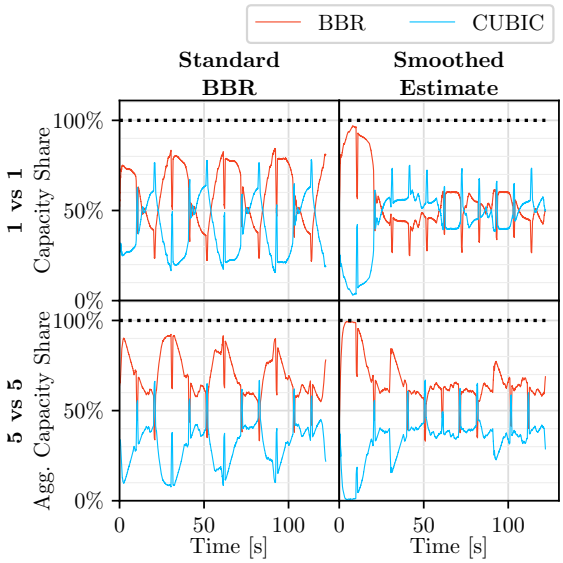

Figure 10: Evaluation of the BBR adaptation using a moving average of the minimum-RTT estimate ($\tau^{\min}$) with $\theta = 1/6$). As a result of the adaptation, the oscillation is successfully dampened.

The stability of $\overline{w}$ depends on the slope of $w^{\leftarrow}$ near the equilibrium. If the slope satisfies $\frac{\partial w^{\leftarrow}}{\partial w} < -1$, trajectories are pushed away rather than attracted. Formally, in that case, there exists a neighborhood Ω around $\overline{w}$ such that all trajectories entering Ω eventually leave it again. Hence, under the stated condition, the long-term equilibrium is unstable. □

This instability has practical implications: It means that the long-term equilibrium cannot be used to predict aggregate throughput as in Fig. 3, since the system may never settle at $\overline{w}$. Nevertheless, the formal characterization of instability enables new predictions that earlier BBR and CUBIC models cannot provide [36, 43, 48, 50]. In particular, we can now predict the frequency of oscillations (§5.5) and the degree of unfairness between BBR and CUBIC during these oscillations (§6).

Interestingly, the instability condition in Theorem 3 does not involve feedback delay. Traditionally, delay is seen as the main source of instability in congestion control [31, 46]. Here, oscillations arise directly from the idealized dynamics of Eqs. (DE1)–(DE3), even without delay. Incorporating feedback delay remains an important direction for future work, as it may reveal additional modes of instability. However, §5.5 shows that our delay-free condition already predicts oscillatory behavior with high accuracy.

5.5. Incidence of Oscillation

After leveraging the oscillation model to elicit abstract conditions for oscillation, we now investigate how frequently these conditions are satisified, i.e., how often an unstable neighborhood Ω around the long-term equilibrium $\overline{w}$ exists.

We first note that the unknown update function $w^{\leftarrow}$ can be well approximated by the equilibrium window-update function $\tilde{w}^{\leftarrow}$ around $\overline{w}$, where the unstable neighborhood Ω should exist: Around $w \approx \overline{w}$, the difference between the window size w and its associated short-term equilibrium $\tilde{w}^{\leftarrow}(w)$ shrinks (because $\overline{w} = \tilde{w}^{\leftarrow}(\overline{w}) = w^{\leftarrow}(\overline{w})$). Hence, the congestion window likely manages to converge to the short-term equilibrium, and thus $w^{\leftarrow}(w) \approx \tilde{w}^{\leftarrow}(w)$ for $w \approx \overline{w}$. Therefore, we substitute the unknown function $w^{\leftarrow}$ in Theorem 3 by the known function $\tilde{w}^{\leftarrow}$ for our analysis.

Given this substitution, we evaluate the strictness of the condition in Theorem 3 by testing a range of parameter combinations similar to the experiment configurations from Fig. 6. In particular, we si-

multaneously vary two critical parameters of the configuration. Any configuration includes a bottleneck capacity $C_\ell \in [1, 200]$ Mbps (default: 100 Mbps), a path propagation delay $\tau^{\mathrm{p}} \in [1, 100]$ ms (default: 40 ms), the bottleneck-link propagation delay τ_ℓ^{p} in percent of τ^{p} (default: 25%), and the bottleneck buffer capacity $B_\ell \in [0.1, 3]$ as a multiple of path BDPs (default: 1.5).

The parameter exploration in Fig. 9 shows that instability is promoted by large values of C_ℓ, τ^{p}, and B_ℓ. Fluid-model simulations, which are highly accurate, confirm the boundary of the unstable region predicted by the oscillation condition from Theorem 3. These simulations were automatically evaluated for convergence of the minimum-RTT estimate $\tau^{\min}$. Importantly, the instability region predicted by Theorem 3 is always contained within the simulation-validated region, consistent with the theorem's status as a sufficient (but not necessary) condition. Thus, while additional factors such as feedback delay (absent from the theorem but present in simulation) can also trigger oscillations, the predicted instability region closely aligns with the simulation-based one, indicating that feedback delay plays only a secondary role.

6. Fairness under Oscillation

Fairness under oscillation depends on the fairness of the *oscillation pattern*, i.e., the evenness of all rate distributions during the oscillation. Formally, this oscillation pattern can be reduced to the series $\{w(t)\}_{t\in\mathbb{N},t\geq 0}$ of CUBIC window sizes from Eq. (21).

This oscillation pattern has a worst-case form, which is found in §6.1. From this worst-case pattern, fairness bounds are computed and experimentally validated in §6.2.

6.1. Bounding the Oscillation Pattern

The fairness of the oscillation pattern can be lower-bounded by maximizing the *amplitude* of the oscillation pattern, i.e., the variance of $x^{\mathrm{C}}(t)$ and $x^{\mathrm{B}}(t)$ over time:

Theorem 4. ***Worst-Case Oscillation Pattern.*** *Given oscillation with maximum amplitude, the CUBIC flow oscillates between the congestion-window sizes $\hat{w}_0 = \tilde{w}^{\leftarrow}(w^{>})$ and $\hat{w}_1 = \tilde{w}^{\leftarrow}(w^{<})$ when competing with a BBR flow ($\hat{w}_0 < \hat{w}_1$).*

Proof Sketch. The proof in §Appendix E rests on two observations regarding the oscillation amplitude. First, this oscillation amplitude corresponds to the window-size changes in the update intervals, i.e., the difference between the window size w at the start of the interval and the convergence result $w^{\leftarrow}(w)$ at the end of the interval (cf. Fig. 8). This difference $|w - w^{\leftarrow}(w)|$ is upper-bounded by $|w - \tilde{w}^{\leftarrow}(w)|$, i.e., the difference for complete convergence to the short-term equilibrium. Hence, the amplitude of the oscillation is maximized by assuming $w^{\leftarrow} = \tilde{w}^{\leftarrow}$. Second, the oscillation amplitude correlates with the size of the unstable neighborhood Ω around the long-term equilibrium $\overline{w}$, as the oscillation pattern typically involves a window-size change across Ω, e.g., from $w(t) < \omega_0$ to $w(t+1) > \omega_1$. In the feasible maximum, Ω covers the entire decreasing part of $\tilde{w}^{\leftarrow}$.

Under these two assumptions, the oscillation corresponds to a *limit cycle*, cyclically revisiting the window sizes $\hat{w}_0 = \tilde{w}^{\leftarrow}(w^{>})$ and $\hat{w}_1 = \tilde{w}^{\leftarrow}(w^{<})$, where $[w^{<}, w^{>}]$ is the finite value range of $\tilde{w}^{\leftarrow}$. This limit cycle is *sound* for the process in Eq. (21), i.e., $\tilde{w}^{\leftarrow}(\hat{w}_0) = \hat{w}_1$ and $\tilde{w}^{\leftarrow}(\hat{w}_1) = \hat{w}_0$, Moreover, the limit cycle is *attractive*, i.e., the process in Eq. (21) eventually enters the limit cycle. □

While difficult to interpret in this form, Theorem 4 allows to compute the worst-case fairness bounds in the following section.

6.2. Computing Fairness Bounds

In the following, we compute and validate fairness bounds for specific network configurations. In particular, we test a range of 27 configurations, which are variations of the experiment settings in §3.1.1 regarding bottleneck-link capacity C_ℓ, path-propagation delay τ^{p}, and buffer capacity B_ℓ. These Mininet experiments result in 120-second traces (cf. Fig. 11).

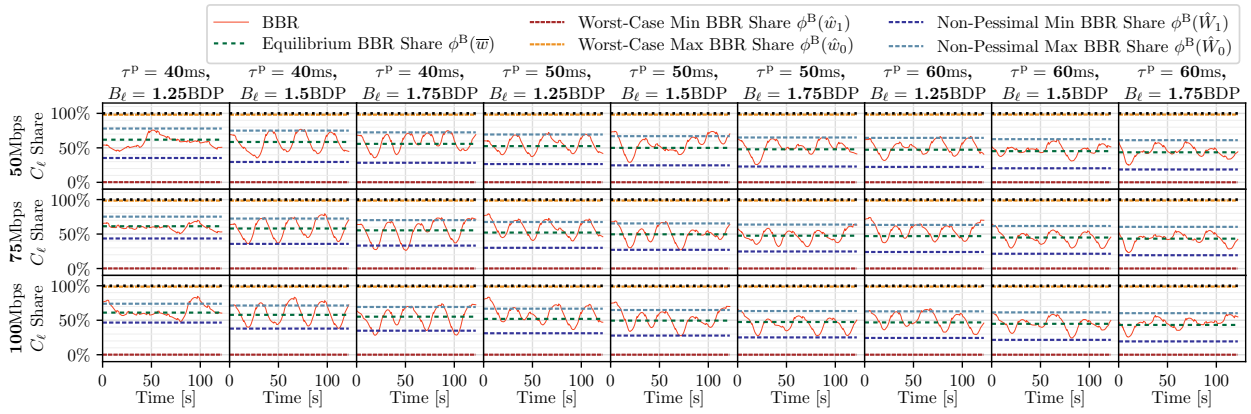

Figure 11: Experimental validation of fairness bounds (cf. §6) (1 flow per CCA).

6.2.1. Worst-Case Bounds

For each of these configurations, we find the worst-case oscillation pattern from Theorem 4. In this oscillation pattern, the CUBIC congestion-window size alternates between two values $\hat{w}_0$ and $\hat{w}_1$ at every RTT-probing step. These congestion-window sizes constitute the *extreme points* of the oscillation: $\hat{w}_0$ is the smallest congestion-window size attained by the CUBIC flow during the oscillation, whereas $\hat{w}_1$ is the largest window size. Hence, $x^{C}(\hat{w}_0) = \hat{w}_0/\overline{\tau}_k$ is the minimal attained CUBIC rate, whereas $x^{C}(\hat{w}_1)$ is maximal.

For BBR, the maximum sending rate is (symmetric for $\hat{w}_1$):

$$x^{B}(\hat{w}_0) = \beta(\hat{w}_1) \cdot \max\left(\chi, C_\ell - \frac{x^{C}(\hat{w}_0)}{\alpha(\hat{w}_1)}\right), \tag{23}$$

which is based on the BBR equilibrium conditions from Lemma 2, because $\hat{w}_0$ and $\hat{w}_1$ represent short-term equilibria. Note that the minimum-RTT estimate (and thus also the strengths α and β) of a BBR flow is based on the CUBIC congestion-window size at the previous RTT-probing step, which is $\hat{w}_1$ when the current congestion-window size is $\hat{w}_0$.

Based on these derived sending rates, we also identify the maximum BBR capacity share:

$$\phi^{B}(\hat{w}_0) = \frac{x^{B}(\hat{w}_0)}{x^{C}(\hat{w}_0) + x^{B}(\hat{w}_0)}. \tag{24}$$

The minimum BBR share $\phi^{B}(\hat{w}_1)$ is found analogously.

To validate these bounds, we compare the theoretically derived bounds to the experimentally found oscillation patterns in Fig. 11. For bound correctness, the oscillation pattern of the BBR flow is supposed to be contained within these bounds, which is clearly true. However, the worst-case bounds are relatively loose, as they are derived with worst-case assumptions, which are overly pessimistic for the settings in Fig. 11.

6.2.2. Non-Pessimal Bounds

As described above, worst-case fairness is realized if the BBR/CUBIC competition dynamics always converge completely to the current short-term equilibrium between RTT probing steps. In reality, however, convergence often takes more than 10 seconds, and is thus often incomplete at the time of the next RTT-probing step. Given this insight on incomplete convergence, we can find approximate non-pessimal fairness bounds $\phi^{B}(\hat{W}_0)$ and $\phi^{B}(\hat{W}_1)$, where:

$$\hat{W}_0 = W(\overline{w}, 0) \qquad \hat{W}_1 = W(\overline{w}, 10) \tag{25}$$

and W is the CUBIC window-growth function from Eq. (1). The non-pessimal bounds are informed by insights on the convergence behavior of the CUBIC state variables ($w^{\max}$ and s) from Theorems 2 and

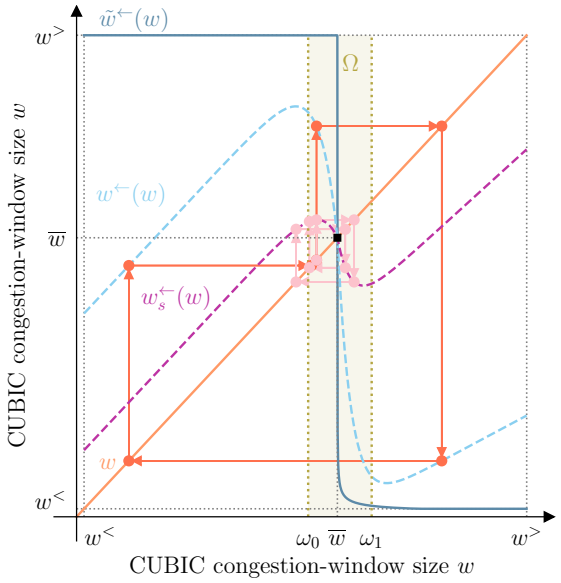

Figure 12: Theoretical explanation of oscillation reduction by smoothed-estimate adaptation.

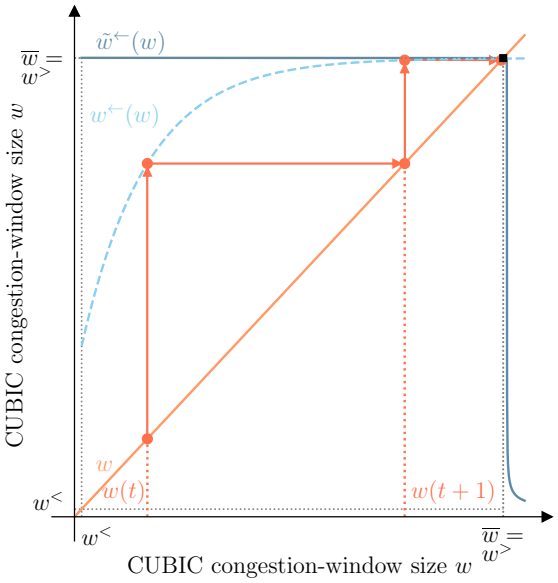

Figure 13: Theoretical explanation of oscillation elimination by BBRv2 and BBRv3.

3: These insights suggest that (1) the CUBIC state variable $w^{\max}$ is usually close to the CUBIC window size $\overline{w}$ from the long-term equilibrium ($w^{\max} \approx \overline{w}$), and (2) the CUBIC window-growth duration s is usually between 0 seconds (as it cannot be negative) and 10 seconds (i.e., the duration between RTT-probing steps, where loss typically occurs), i.e., $s \in [0, 10]$. The full derivation is presented in §Appendix F.

The non-pessimal bounds $\phi^{\mathrm{B}}(\hat{W}_0)$ and $\phi^{\mathrm{B}}(\hat{W}_1)$ are also shown in Fig. 11. These bounds are sometimes violated due to their approximate nature, but predict the range of oscillating BBR-share values better than the worst-case bounds.

7. Preventing Oscillation

To prevent unfairness from oscillation, we evaluate different countermeasures, and explain their effects by means of our control-theoretic framework.

7.1. Smoothed Minimum-RTT Estimate

In the analysis from §5.4, we find that the long-term BBR/ CUBIC dynamics oscillate because the update function $w^{\leftarrow}$ of the CUBIC congestion-window size w is too steep around the long-term equilibrium $\overline{w}$. This steepness is caused by the fact that the minimum-RTT estimate $\tau^{\min}$ (and thus the probing strength α and the window-update function $w^{\leftarrow}$) of the BBR flows is highly sensitive to the CUBIC congestion-window size w at the time of RTT probing. To reduce this sensitivity and thereby reduce oscillation, we use a classic control-theoretic idea: We slow down the adjustment of the minimum-RTT estimate to new RTT measurements using a moving average. Formally, an RTT-probing step at time t updates the minimum-RTT estimate $\tau^{\min}$ as follows:

$$\tau^{\min}(t) = \theta \cdot \left(\tau_i^{\mathrm{p}} + \frac{q_\ell^-(t)}{C_\ell} \right) + (1-\theta) \cdot \tau^{\min}(t-10) \tag{26}$$

where θ denotes the adaptation speed of $\tau^{\min}$ to the most recently measured RTT (Eq. (15)).

Indeed, this smoothing of the minimum-RTT estimate can dampen, but not completely eliminate oscillation (Fig. 10). Figure 12 explains this effect for the situation of Fig. 8: As the window-update function $w^{\leftarrow}$

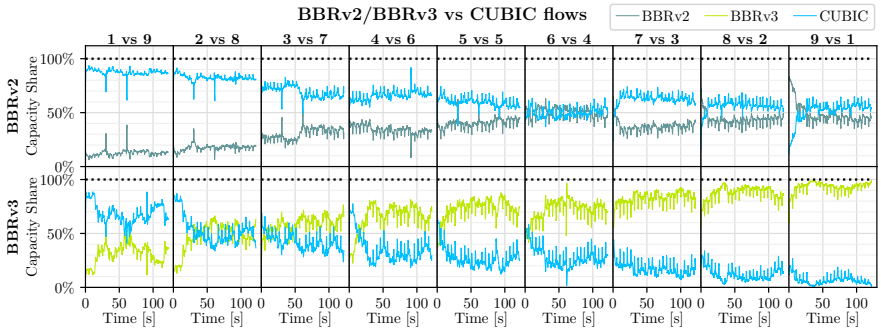

Figure 14: Competition between BBRv2/BBRv3 and CUBIC (Aggregate capacity share by CCA).

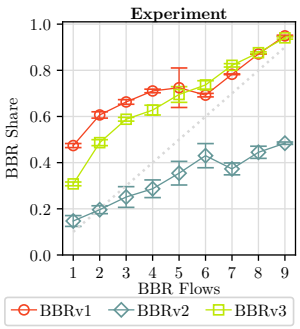

Figure 15: Capacity shares obtained by BBR versions.

is transformed into the update function $w_s^{\leftarrow}$, the original oscillation trajectory (in orange) is reduced to a much more narrow trajectory (in rose), corresponding to oscillation with lower amplitude.

However, we note that this smoothing approach reduces responsiveness when a path change alters the propagation delay, which may be acceptable in fixed networks, but is problematic in mobile networks. We also implement and evaluate two alternative BBR adaptations in §Appendix G, but these adaptations have less desirable effects.

7.2. BBRv2 and BBRv3

Similarly to the smoothed-estimate adaptation in the preceding section, BBRv2 eliminates oscillation by reducing the sensitivity of the BBR rate on the minimum-RTT estimate $\tau^{\min}$: While BBRv1 constrains the inflight volume only with the BBR congestion-window size of $2x^{\text{btl}}\tau^{\min}$, BBRv2 constrains this inflight volume (and thus the sending rate) more strongly, i.e., by multiplying the minimum-RTT estimate $\tau^{\min}$ with a factor lower than $2x^{\text{btl}}$. In particular, BBRv2 has a long-term inflight bound (*inflight_hi*), which is at most $5/4 \cdot x^{\text{btl}}\tau^{\min}$, and a short-term inflight bound (*inflight_lo*), which is at most $x^{\text{btl}}\tau^{\min}$. Both these bounds are even further reduced if loss occurs frequently, as in the competition with CUBIC.

These new inflight bounds alter the formulation of the strengths α and β, as shown by Scherrer et al. [43]:

$$\text{Limited by } \textit{inflight_hi}\text{:}\quad \alpha' \overset{[43]}{=} \frac{5}{4}\cdot\min\left(1,\tau^{\min}/\tau\right) \leq \min\left(\frac{5}{4},2\tau^{\min}/\tau\right) \overset{(12)}{=} \alpha \tag{27}$$

$$\text{Limited by } \textit{inflight_lo}\text{:}\quad \beta' \overset{[43]}{=} \min\left(1,\tau^{\min}/\tau\right) \leq \min\left(1,2\tau^{\min}/\tau\right) \overset{(2)}{=} \beta \tag{28}$$

As $\alpha' \leq \alpha$ and $\beta' \leq \beta$, the sending rate in BBRv2 is less strongly affected by varying minimum-RTT estimates than in BBRv1, and oscillation is prevented. Fig. 13 illustrates this effect theoretically: Computing the equilibrium window-update function $\tilde{w}^{\leftarrow}$ with α' and β' lowers the 'maximum plateau' at $w^{>}$. Hence, a different intersection point (long-term equilibrium) $\overline{w} = w^{>}$ results, crucially located on the plateau, which allows convergence. The convergence is confirmed by the experiments in Fig. 14.

However, the BBRv2 features that suppress oscillation have two drawbacks. First, BBRv2 flows might obtain less than the fair bandwidth share. This unfairness is reflected by (i) the theoretical observation that the CUBIC window size $\overline{w}$ in the long-term equilibrium of Fig. 13 is stable and relatively high, suggesting a low BBR capacity share in equilibrium, and (ii) the experimental observation that most cases in Fig. 15 show sub-proportional throughput for BBRv2. Second, the relatively static inflight bounds of BBRv2 slow down the discovery of newly available bandwidth [53].

To remedy these issues, Google has recently released BBRv3, which is largely equal to BBRv2, but more aggressively probes for additional bandwidth [10]. Due to this higher aggressiveness, BBRv3 obtains an over-proportional bandwidth share (cf. Fig. 15), and is thus similarly unfair as BBRv1, albeit stable.

In summary, BBRv 2 and BBRv3 solve the instability problem of BBRv1, but still do not achieve perfect per-flow fairness. Designing a BBR version that is stable *and* fair is an interesting task for future work, and can benefit from our control-theoretic methodology.

8. Related Work

Most relevant related work. Our work has a close connection to the two previous steady-state models of BBR/ CUBIC competition [50, 36], and the fluid models for CUBIC [48] and BBR [43]. Another highly relevant recent work is by Arun et al. [2], who investigate the delay oscillations caused by delay-bounding CCAs (such as BBR) and loss-based CCAs (such as CUBIC) in *homogeneous* settings. In particular, they find that the amplitude of these delay oscillations should exceed the random, non-congestive jitter that is expected, in order to avoid starvation of flows measuring a distorted RTT. Our work complements this analysis by investigating oscillation in *heterogeneous* settings, i.e., given CCA competition. Moreover, we identify an additional condition for BBR starvation involving delay measurements, namely Lemma 3.

Congestion-control models. Congestion-control algorithms have been analyzed with a wide range of modeling techniques [46, 39].

For example, *steady-state models* describe only the equilibrium of CCA execution in terms of network metrics. Most influentially, Mathis et al. [32] and Padhye et al. [40] provide closed-form functions for long-term Reno throughput based on RTT and packet loss; their methodology has been extended to short-lived flows and other CCAs [12, 28, 4].

In contrast, *dynamic models* represent the full CCA behavior over time. This evolution is sometimes represented in discrete time [1, 3, 54, 41], but more often in continuous time by fluid models. Specific fluid models exist for Reno [31, 37], Vegas [5], CUBIC [48], and BBRv1 and v2 [43]. While these models have been applied to analyze fairness and stability [26, 25, 24, 30], our work is the first to theoretically investigate inter-CCA fairness with a dynamic fluid model.

BBR. Motivated by the excessive queuing of loss-based CCAs (e.g., Reno [15], CUBIC [18]) and competitiveness issues of latency-based CCAs (e.g., Vegas [6]), Google proposed the BBR CCA in 2017 [8]. BBR was enabled for YouTube soon afterwards [9], and was used by around 40% of Internet traffic in 2019 [35]. Given that BBR competes with other CCAs in the Internet, its fairness towards other CCAs has received much attention. In a first independent study, Hock et al. [19] demonstrate that BBR is over-aggressive against loss-based CCAs for settings with small buffers, and under-aggressive given large buffers. In these large buffers, the BBR congestion window restricts the BBR sending rate, which is confirmed by follow-up work [44, 13, 47, 52]. This insight about BBR fairness triggered the release of BBRv2 [11], which is less aggressive, but also less responsive than BBRv1 [53, 27, 38, 45]. Finally, the sub-optimal assertiveness and responsiveness of BBRv2 led to the release of BBRv3 in 2023 [10].

Congestion-control fairness. In congestion-control research, fairness is typically measured by some aggregation (e.g., Jain fairness index [23]) of the throughput-share distribution across flows on a bottleneck link [13, 8, 50, 36, 44, 19]. Alternative fairness measures focus on flow-completion times [14], on quality of experience (QoE) [20], or on compatibility with CCAs already deployed in the Internet [49], or avoid flows as entities of the fairness definition [7].

9. Conclusion

Dynamic fluid models have an under-explored potential for generating interpretable and even provable insights into complex congestion-control phenomena. To tap into this potential, we leverage these models for a theoretical stability analysis of BBR/CUBIC competition. Through this control-theoretic analysis, we provide a mathematical explanation for the oscillation that regularly occurs in BBR/CUBIC competition. Moreover, we derive quantitative conditions on networks that are susceptible to oscillation, and quantitative bounds on the unfairness caused by extreme rate distributions during the oscillation. While these extreme rate distributions are transient, they are substantially more unfair than the long-term average rate distribution, and thus also matter for the fairness among short flows. Finally, our control-theoretic framework also explains the effects and shortcomings of different stabilizing adaptations of BBR.

By pioneering the use of theoretical stability analysis for inter-CCA competition, this paper opens numerous avenues for future research. While our analysis is extensive, it represents only the beginning of

what control theory can offer. The application of advanced control-theoretic techniques to hybrid CCA fluid models has the potential to uncover even deeper insights. Notably, we see significant promise in Lyapunov functions for understanding which initial configurations allow convergence to the equilibria (global asymptotic stability and region of attraction), the Laplace transform for modeling time-delay effects, and robust-controller design for rigorously eliminating oscillations in a broad range of network settings.

Although being extensible in these many ways, our analysis already now provides practically relevant insights. By characterizing when oscillations and unfairness arise, our results can inform the design and parameter tuning of congestion-control algorithms, and guide practitioners in anticipating performance issues in heterogeneous deployments.

Acknowledgements

We gratefully acknowledge funding from ETH Zurich, and from the German Research Foundation (DFG) for project 'Algorithms for Flexible Networks (FlexNets)' (Grant 470029389). Moreover, we thank Andrés Ferragut for shepherding, and the anonymous reviewers for valuable suggestions.

References

[1] Aditya Akella, Srinivasan Seshan, Richard Karp, Scott Shenker, and Christos Papadimitriou. Selfish behavior and stability of the Internet: A game-theoretic analysis of TCP. *ACM SIGCOMM Computer Communication Review*, 32(4):117–130, 2002.

[2] Venkat Arun, Mohammad Alizadeh, and Hari Balakrishnan. Starvation in end-to-end congestion control. In *Proceedings of the ACM SIGCOMM 2022 Conference*, pages 177–192, 2022.

[3] Venkat Arun, Mina Tahmasbi Arashloo, Ahmed Saeed, Mohammad Alizadeh, and Hari Balakrishnan. Toward formally verifying congestion control behavior. In *Proceedings of the ACM SIGCOMM 2021 Conference*, pages 1–16, 2021.

[4] Wei Bao, Vincent WS Wong, and Victor CM Leung. A model for steady state throughput of TCP CUBIC. In *IEEE Global Telecommunications Conference GLOBECOM 2010*, pages 1–6. IEEE, 2010.

[5] Thomas Bonald. *Comparison of TCP Reno and TCP Vegas via fluid approximation.* PhD thesis, INRIA, 1998.

[6] Lawrence S Brakmo, Sean W O'Malley, and Larry L Peterson. TCP Vegas: New techniques for congestion detection and avoidance. In *Proceedings of the conference on Communications architectures, protocols and applications*, pages 24–35, 1994.

[7] Bob Briscoe. Flow rate fairness: Dismantling a religion. *ACM SIGCOMM Computer Communication Review*, 37(2):63–74, 2007.

[8] Neal Cardwell, Yuchung Cheng, C Stephen Gunn, Soheil Hassas Yeganeh, and Van Jacobson. BBR: congestion-based congestion control. *Communications of the ACM*, 60(2):58–66, 2017.

[9] Neal Cardwell, Yuchung Cheng, C Stephen Gunn, Soheil Hassas Yeganeh, Ian Swett, Jana Iyengar, Victor Vasiliev, and Van Jacobson. BBR congestion control: IETF 99 update. In *Presentation in ICCRG at IETF 99*, 2017. URL: `https://datatracker.ietf.org/meeting/99/materials/slides-99-iccrg-iccrg-presentation-2-00.pdf`.

[10] Neal Cardwell, Yuchung Cheng, Kevin Yang, David Morley, Soheil Hassas Yeganeh, Priyaranjan Jha, Yousuk Seung, and Van Jacobson. BBRv3: Algorithm Bug Fixes and Public Internet Deployment. `https://datatracker.ietf.org/meeting/117/materials/slides-117-ccwg-bbrv3-algorithm-bug-fixes-and-public-internet-deployment-00`, 2023.

[11] Neal Cardwell, Yuchung Cheng, S Hassas Yeganeh, Ian Swett, Victor Vasiliev, Priyaranjan Jha, Yousuk Seung, Matt Mathis, and Van Jacobson. BBRv2: A model-based congestion control. In *Presentation in ICCRG at IETF 104th meeting*, 2019.

[12] Neal Cardwell, Stefan Savage, and Thomas Anderson. Modeling TCP latency. In *Proceedings of IEEE INFOCOM 2000*, volume 3, pages 1742–1751. IEEE, 2000.

[13] Mo Dong, Tong Meng, Doron Zarchy, Engin Arslan, Yossi Gilad, Brighten Godfrey, and Michael Schapira. PCC Vivace: Online-learning congestion control. pages 343–356, 2018.

[14] Nandita Dukkipati and Nick McKeown. Why flow-completion time is the right metric for congestion control. *ACM SIGCOMM Computer Communication Review*, 36(1):59–62, 2006.

[15] Kevin Fall and Sally Floyd. Simulation-based comparisons of Tahoe, Reno and SACK TCP. *ACM SIGCOMM Computer Communication Review*, 26(3):5–21, 1996.

[16] Jose Gomez, Elie Kfoury, Jorge Crichigno, Elias Bou-Harb, and Gautam Srivastava. A performance evaluation of TCP BBRv2 alpha. In *2020 43rd International Conference on Telecommunications and Signal Processing (TSP)*, pages 309–312. IEEE, 2020.

[17] John Guckenheimer and Philip Holmes. *Nonlinear oscillations, dynamical systems, and bifurcations of vector fields (Section 3.2)*, volume 42. Springer Science & Business Media, 2013.

[18] Sangtae Ha, Injong Rhee, and Lisong Xu. CUBIC: a new TCP-friendly high-speed TCP variant. *ACM SIGOPS operating systems review*, 42(5):64–74, 2008.

[19] Mario Hock, Roland Bless, and Martina Zitterbart. Experimental evaluation of BBR congestion control. pages 1–10. IEEE, 2017.

[20] Tobias Hoßfeld, Lea Skorin-Kapov, Poul E Heegaard, and Martin Varela. Definition of QoE fairness in shared systems. *IEEE Communications Letters*, 21(1):184–187, 2016.

[21] Gerard Iooss and Moritz Adelmeyer. *Topics in bifurcation theory and applications*, volume 3. World Scientific, 1998.

[22] Van Jacobson, Neal Cardwell, Yuchung Cheng, and Soheil Hassas Yeganeh. BBRv1 Source Code. `https://github.com/torvalds/linux/blob/master/net/ipv4/tcp_bbr.c`, 2023. Accessed on 2023-03-28.

[23] Raj Jain, Arjan Durresi, and Gojko Babic. Throughput fairness index: An explanation. In *ATM Forum contribution*, volume 99, 1999.

[24] Ramesh Johari and David Kim Hong Tan. End-to-end congestion control for the internet: Delays and stability. *IEEE/ACM Transactions on networking*, 9(6):818–832, 2001.

[25] Frank Kelly. Fairness and stability of end-to-end congestion control. *European journal of control*, 9(2-3):159–176, 2003.

[26] Frank P Kelly, Aman K Maulloo, and David Kim Hong Tan. Rate control for communication networks: shadow prices, proportional fairness and stability. *Journal of the Operational Research society*, 49(3):237–252, 1998.

[27] Elie F Kfoury, Jose Gomez, Jorge Crichigno, and Elias Bou-Harb. An emulation-based evaluation of TCP BBRv2 alpha for wired broadband. *Computer Communications*, 161:212–224, 2020.

[28] Anurag Kumar. Comparative performance analysis of versions of TCP in a local network with a lossy link. *Ieee/Acm Transactions on Networking*, 6(4):485–498, 1998.

[29] Bob Lantz, Nikhil Handigol, Brandon Heller, and Vimal Jeyakumar. Introduction to Mininet. `https://github.com/mininet/mininet/wiki/Introduction-to-Mininet`, 2021.

[30] Yong Liu, Francesco Lo Presti, Vishal Misra, Don Towsley, and Yu Gu. Fluid models and solutions for large-scale IP networks. pages 91–101, 2003.

[31] Steven H Low, Fernando Paganini, and John C Doyle. Internet congestion control. *IEEE control systems magazine*, 22(1):28–43, 2002.

[32] Matthew Mathis, Jeffrey Semke, Jamshid Mahdavi, and Teunis Ott. The macroscopic behavior of the TCP congestion avoidance algorithm. *ACM SIGCOMM Computer Communication Review*, 27(3):67–82, 1997.

[33] MathWorks. Symbolic Math Toolbox. `https://ch.mathworks.com/products/symbolic.html`, 2023.

[34] Robert McMahon. iPerf. `https://sourceforge.net/projects/iperf2/`, 2021.

[35] Ayush Mishra, Xiangpeng Sun, Atishya Jain, Sameer Pande, Raj Joshi, and Ben Leong. The great internet TCP congestion control census. *Proceedings of the ACM on Measurement and Analysis of Computing Systems*, 3(3):1–24, 2019.

[36] Ayush Mishra, Wee Han Tiu, and Ben Leong. Are we heading towards a BBR-dominant Internet? In *Proceedings of the 22nd ACM Internet Measurement Conference (IMC)*, pages 538–550, 2022.

[37] Vishal Misra, Wei-Bo Gong, and Don Towsley. Fluid-based analysis of a network of AQM routers supporting TCP flows with an application to RED. In *Proceedings of the ACM Conference on Applications, Technologies, Architectures, and Protocols for Computer Communication (SIGCOMM)*, pages 151–160, 2000.

[38] Aarti Nandagiri, Mohit P Tahiliani, Vishal Misra, and KK Ramakrishnan. BBRv1 vs BBRv2: Examining performance differences through experimental evaluation. In *2020 IEEE International Symposium on Local and Metropolitan Area Networks (LANMAN*, pages 1–6. IEEE, 2020.

[39] Jörgen Olsén. *Stochastic modeling and simulation of the TCP protocol*. PhD thesis, Department of Mathematics, Uppsala University, 2003.

[40] Jitendra Padhye, Victor Firoiu, Don Towsley, and Jim Kurose. Modeling TCP throughput: A simple model and its empirical validation. In *Proceedings of the ACM SIGCOMM'98 conference on Applications, technologies, architectures, and protocols for computer communication*, pages 303–314, 1998.

[41] Sudheer Poojary and Vinod Sharma. Analytical model for congestion control and throughput with TCP CUBIC connections. In *2011 IEEE Global Telecommunications Conference-GLOBECOM 2011*, pages 1–6. IEEE, 2011.

[42] I Rhee, L Xu, S Ha, A Zimmermann, L Eggert, and R Scheffenegger. RFC 8312: CUBIC for Fast Long-Distance Networks, 2018.

[43] Simon Scherrer, Markus Legner, Adrian Perrig, and Stefan Schmid. Model-based insights on the performance, fairness, and stability of BBR. In *Proceedings of the 22nd ACM Internet Measurement Conference (IMC)*, pages 519–537, 2022.

[44] Dominik Scholz, Benedikt Jaeger, Lukas Schwaighofer, Daniel Raumer, Fabien Geyer, and Georg Carle. Towards a deeper understanding of TCP BBR congestion control. In *Proceedings of the IFIP Networking Conference (IFIP Networking) and Workshops*, pages 1–9. IEEE, 2018.

[45] Yeong-Jun Song, Geon-Hwan Kim, Imtiaz Mahmud, Won-Kyeong Seo, and You-Ze Cho. Understanding of BBRv2: Evaluation and comparison with BBRv1 congestion control algorithm. *IEEE Access*, 9:37131–37145, 2021.

[46] Rayadurgam Srikant. *The mathematics of Internet congestion control*. Springer Science & Business Media, 2004. doi:10.1007/978-0-8176-8216-3.

[47] Belma Turkovic, Fernando A Kuipers, and Steve Uhlig. Fifty shades of congestion control: A performance and interactions evaluation. *arXiv preprint arXiv:1903.03852*, 2019.

[48] Gayane Vardoyan, CV Hollot, and Don Towsley. Towards stability analysis of data transport mechanisms: A fluid model and its applications. *IEEE/ACM Transactions on Networking*, 29(4):1730–1744, 2021.

[49] Ranysha Ware, Matthew K Mukerjee, Srinivasan Seshan, and Justine Sherry. Beyond jain's fairness index: Setting the bar for the deployment of congestion control algorithms. In *Proceedings of the 18th ACM Workshop on Hot Topics in Networks*, pages 17–24, 2019.

[50] Ranysha Ware, Matthew K Mukerjee, Srinivasan Seshan, and Justine Sherry. Modeling BBR's interactions with loss-based congestion control. In *Proceedings of the Internet Measurement Conference*, pages 137–143, 2019.

[51] Stephen Wiggins and Martin Golubitsky. *Introduction to applied nonlinear dynamical systems and chaos (Chapter 18)*, volume 2. Springer, 2003.

[52] Xiaokun Xu and Mark Claypool. Measurement of cloud-based game streaming system response to competing TCP CUBIC or TCP BBR flows. In *Proceedings of the 22nd ACM Internet Measurement Conference (IMC)*, pages 305–316, 2022.

[53] Furong Yang, Qinghua Wu, Zhenyu Li, Yanmei Liu, Giovanni Pau, and Gaogang Xie. BBRv2+: Towards balancing aggressiveness and fairness with delay-based bandwidth probing. *Computer Networks*, 206:108789, 2022.

[54] Doron Zarchy, Radhika Mittal, Michael Schapira, and Scott Shenker. Axiomatizing congestion control. *Proceedings of the ACM on Measurement and Analysis of Computing Systems*, 3(2):1–33, 2019.

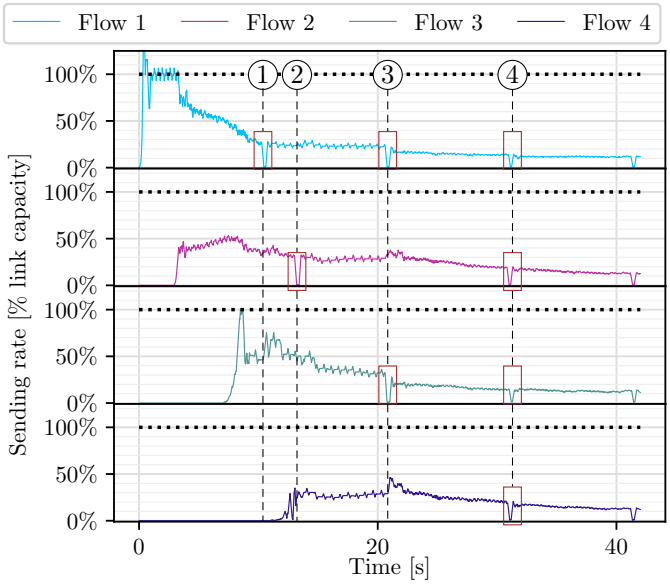

Figure A.16: Self-synchronization of RTT probing (highlighted with red rectangles) among 4 BBR flows.

Appendix A. Oscillation of multiple flows

The explanation of the oscillation mechanism in §3.2 applies to the case with a single flow per CCA. We now explain how and why the mechanism generalizes to multiple flows.

The generalization to multiple CUBIC flows is straightforward: The explanation in §3.2 is equally valid for multiple CUBIC flows, with the slight adaptation that the *aggregate* congestion-window size of all CUBIC flows affects the minimum-RTT estimate $\tau^{\min}$ of a BBR flow.

Interestingly, multiple BBR flows also behave analogously to a single BBR flow for the purpose of oscillation because BBR flows synchronize their RTT-probing steps. This synchronization has been documented by previous work [8, 44], and is experimentally confirmed in Fig. A.16. In that experiment, 4 BBR flows are initiated sequentially with 4-second delays, and compete with 6 CUBIC flows (not pictured). The BBR flow 1 performs the first RTT probing at Time ①, which shrinks the queue and reduces the RTT. In fact, the RTT is reduced enough such that Flow 3 measures a new minimum RTT. Hence, Flow 1 and Flow 3 start the reset timers of their minimum-RTT estimates at the same time, and therefore simultaneously probe the RTT at Time ③ = ① +10 seconds. At this Time ③, also the remaining two flows 2 and 4 become synchronized with flows 1 and 3 such that all flows perform a simultaneous RTT probing at Time ④.

Finally, note that oscillation does not necessarily arise in a multiple-flow scenario if the CCA distribution is very unequal, e.g., for 9 BBR flows and 1 CUBIC flow in Fig. 4. In this case, the single CUBIC flow never manages to inflate the minimum-RTT estimate of the BBR flows, and hence the rate distribution is largely static.

Appendix B. Proof of Theorem 1: Short-Term Equilibrium

In the following, we consistently write $\tilde{s}$ for $\tilde{s}(\alpha)$, as α is considered fixed throughout the proof (analogously for $\tilde{w}^{\max}$ and $\tilde{x}^{\text{btl}}$)

The CUBIC maximum window $\tilde{w}^{\max}$ in equilibrium (and by extension also the CUBIC equilibrium rate $\tilde{x}^{\text{C}}$) is directly determined by the CUBIC window-growth duration $\tilde{s}$ in equilibrium:

$$\tilde{w}^{\max} \overset{(7)}{=} \frac{c}{b}\tilde{s}^3 \iff \tilde{x}^{\text{C}} = \frac{c\tilde{s}^3}{b\tilde{\tau}_k}. \tag{B.1}$$

The short-term equilibrium delay $\tilde{\tau}_k$ also matches the general equilibrium delay $\overline{\tau}_k$ from Eq. (10) because also the short-term equilibrium involves non-zero loss and thus a full buffer. To characterize the equilibrium completely, it remains to determine $\tilde{s}$ and $\tilde{x}^{\text{btl}}$, which we achieve with a case distinction on α.

Appendix B.1. Low Probing Strength: $\alpha \leq 1$

We first consider the case $\alpha \leq 1$. According to Lemma 3, $\tilde{x}_i^{\text{btl}}$ must equal the lower bound χ in this case. For $\tilde{x}_i^{\text{btl}} = \chi$, the CUBIC equilibrium condition in Lemma 1 suggests:

$$\begin{aligned} &\frac{b\tilde{\tau}_k}{c\tilde{s}^4} \overset{(9)}{=} 1 - \frac{C_\ell}{\tilde{y}_\ell} \overset{(3)}{=} 1 - \frac{C_\ell}{\beta\tilde{x}^{\text{btl}} + \tilde{x}^{\text{C}}} \underset{\beta=\alpha}{\overset{\text{(B.1)}}{=}} 1 - \frac{C_\ell}{\alpha\chi + \frac{c\tilde{s}^3}{b\tilde{\tau}_k}} \iff \\ &\frac{c^2}{b\tilde{\tau}_k}\tilde{s}^7 - c\left(C_\ell - \alpha\chi\right)\tilde{s}^4 - c\tilde{s}^3 - \alpha b\tilde{\tau}_k\chi = 0, \end{aligned} \tag{B.2}$$

where the polynomial in the last equation corresponds to $\tilde{S}_2(\tilde{s})$ in Eq. (20). Note that $\beta = \alpha$ is implied by $\alpha \leq 1$ (cf. Eqs. (2) and (12)). The septic equation $\tilde{S}_2(s) = 0$ has a unique solution for positive s, which follows from two arguments:

1. *Negativity at 0:* $\tilde{S}_2(0) = -\alpha b\tilde{\tau}_k\chi < 0$.
2. *Strict monotonic increase after monotonic decrease:*

$$\begin{aligned} \exists s' \geq 0 \quad \text{s.t.} \quad &\forall s \in [0, s').\ \tilde{S}_2'(s') \leq 0 \quad \text{and} \\ &\forall s > s'.\ \tilde{S}_2'(s) > 0. \end{aligned} \tag{B.3}$$

The existence of such a unique turning point s' is proven in §Appendix B.3.

Appendix B.2. High Probing Strength: $\alpha > 1$

Conversely, if $\alpha > 1$, $\tilde{x}^{\text{btl}}$ may exceed χ. For this case, we consider the *unrestricted* equilibrium $\hat{x}^{\text{btl}}$, i.e., the equilibrium bottleneck-bandwidth estimate $\tilde{x}^{\text{btl}}$ according to Lemma 2, but without restriction to the domain $[\chi, \infty)$:

$$\hat{x}^{\text{btl}} \overset{(14)}{=} C_\ell - \frac{\tilde{x}^{\text{C}}}{\alpha} \overset{\text{(B.1)}}{=} C_\ell - \frac{c\tilde{s}^3}{\alpha b\tilde{\tau}_k}. \tag{B.4}$$

We now distinguish the cases $\hat{x}^{\text{btl}} \geq \chi$ and $\hat{x}^{\text{btl}} < \chi$.

$\hat{x}^{\text{btl}} \geq \chi$. In this case, the actual equilibrium $\tilde{x}^{\text{btl}}$ matches the unrestricted equilibrium $\hat{x}^{\text{btl}}$. Plugging $\tilde{x}^{\text{btl}} = \hat{x}^{\text{btl}}$ into the CUBIC equilibrium condition from Eq. (9), we obtain:

$$\begin{aligned} &\frac{b\tilde{\tau}_k}{c\tilde{s}^4} \overset{(9)}{=} 1 - \frac{C_\ell}{\beta\tilde{x}^{\text{btl}} + \tilde{x}^{\text{C}}} \underset{\beta=1}{\overset{\text{(B.1)}}{=}} 1 - \frac{C_\ell}{\tilde{x}^{\text{btl}} + \frac{c\tilde{s}^3}{b\tilde{\tau}_k}} \overset{\text{(B.4)}}{\iff} \\ &\frac{(\alpha-1)c^2}{\alpha b\tilde{\tau}_k}\tilde{s}^7 - \frac{(\alpha-1)\,c}{\alpha}\tilde{s}^3 - bC_\ell\tilde{\tau}_k = 0, \end{aligned} \tag{B.5}$$

where the polynomial in the second equation corresponds to $\tilde{S}_1(\tilde{s})$ in Eq. (19). Note that $\beta = 1$ is implied by $\alpha > 1$. Moreover, the uniqueness of the solution to $\tilde{S}_1 = 0$ can be shown similarly as before:

1. *Negativity at 0:* $\tilde{S}_1(0) = -bC_\ell\tilde{\tau}_k < 0$.
2. *Strict monotonic increase after monotonic decrease:*

$$\begin{aligned} \tilde{S}_1'(s) > 0 &\iff \frac{7(\alpha-1)c^2}{\alpha b\tilde{\tau}_k}s^6 - 3\frac{(\alpha-1)\,c}{\alpha}s^2 > 0 \\ &\overset{/s^2}{\iff} \frac{7(\alpha-1)c^2}{\alpha b\tilde{\tau}_k}s^4 - \frac{3\,(\alpha-1)\,c}{\alpha} > 0 \iff s > \sqrt[4]{\frac{3b\tilde{\tau}_k}{7c}}. \end{aligned} \tag{B.6}$$

$\hat{x}^{\text{btl}} < \chi$. This case arises if the equilibrium window-growth duration $\tilde{s}$ is sufficiently high:

$$\begin{aligned} \hat{x}^{\text{btl}} = C_\ell - \frac{c\tilde{s}^3}{\alpha b\tilde{\tau}_k} < \chi \iff \frac{c\tilde{s}^3}{b\tilde{\tau}_k} > \alpha\,(C_\ell - \chi) \\ \iff \tilde{s} > \sqrt[3]{\frac{\alpha b\tilde{\tau}_k}{c}\,(C_\ell - \chi)} =: \hat{s}(\alpha), \end{aligned} \tag{B.7}$$

where $\hat{s}(\alpha)$ is the window-growth duration that leads to

$$\hat{x}^{\text{btl}} = C_\ell - \frac{c\hat{s}(\alpha)^3}{\alpha b\tilde{\tau}_k} = \chi \overset{\geq\chi}{=} \tilde{x}^{\text{btl}}, \tag{B.8}$$

and to a CUBIC equilibrium rate

$$\tilde{x}^{\text{C}} \overset{\text{(B.4)}}{=} \alpha(C_\ell - \hat{x}^{\text{btl}}) \overset{\text{(B.8)}}{=} \alpha(C_\ell - \chi), \tag{B.9}$$

given probing strength α. In order for $\hat{s}(\alpha)$ to be an equilibrium (i.e., $\tilde{s} = \hat{s}(\alpha)$), $\hat{s}(\alpha)$ has to satisfy the CUBIC equilibrium conditions from Lemma 1:

$$\begin{aligned} \frac{b\tilde{\tau}_k}{c\hat{s}(\alpha)^4} \overset{(9)}{=} 1 - \frac{C_\ell}{\beta\tilde{x}^{\text{btl}} + \tilde{x}^{\text{C}}} \underset{\text{(B.9)}}{\overset{\text{(B.8)}}{=}} 1 - \frac{C_\ell}{\chi + \alpha\,(C_\ell - \chi)} \\ \underset{\text{(B.7)}}{\overset{\hat{s}(\alpha)}{\iff}} \frac{\alpha^4(\alpha-1)^3}{(\chi + \alpha(C_\ell - \chi))^3} = \frac{c}{b\tilde{\tau}_k(C_\ell - \chi)^7} \end{aligned} \tag{B.10}$$

Let $\hat{\alpha}$ be the solution in α to Eq. (B.10), which cannot be found analytically in general. However, it must hold that $\hat{\alpha} > 1$, as $\alpha = 1$ yields a zero LHS in Eq. (B.10), which cannot match the non-zero RHS.

At probing strength $\hat{\alpha}$, it holds that $\hat{s}(\hat{\alpha}) = \tilde{s}$. Since $\hat{s}(\alpha)$ is an increasing function of α according to Eq. (B.7), any $\alpha < \hat{\alpha}$ also leads to $\hat{s}(\alpha) < \tilde{s}$, and thus to $\hat{x}^{\text{btl}} < \chi = \tilde{x}^{\text{btl}}$. Hence, for $\alpha < \hat{\alpha}$, $\tilde{x}^{\text{C}}$ is found by solving $\tilde{S}_2$, i.e., as for $\alpha \leq 1$. We thus arrive at the condition on α in Theorem 1.

Appendix B.3. Uniqueness of Turning Point for $\tilde{S}_2$

We note that the turning point s' of $\tilde{S}_2$ in Eq. (B.2) should be a unique root of the first derivative $\tilde{S}_2'$, where

$$\tilde{S}_2'(s) = \frac{7c^2}{b\tilde{\tau}_k}s^6 - 4c\,(C_\ell - \alpha\chi)\,s^3 - 3cs^2. \tag{B.11}$$

Appendix B.3.1. Strict convexity above critical value s'''

To find the area in which $\tilde{S}_2'$ is strictly convex, we solve the following inequality for the second derivative of $\tilde{S}_2'$:

$$\tilde{S}_2'''(s) > 0 \iff \frac{210c^2}{b\tilde{\tau}_k}s^4 - 24c\,(C_\ell - \alpha\chi)\,s > 0 \tag{B.12}$$

$$\overset{/s}{\iff} \frac{210c^2}{b\tilde{\tau}_k}s^3 - 24c\,(C_\ell - \alpha\chi) > 0 \tag{B.13}$$

The division by s is admissible because we only consider $s > 0$. To identify s''', we note that the LHS in Eq. (B.13) increases from non-positive to positive with s if $C_\ell > \alpha\chi$, and is consistently positive for all $s > 0$ in the rare case where $C_\ell \leq \alpha\chi$. Hence, we arrive at the following value for s''', marking the start of the convex area of $\tilde{S}_2'$:

$$s''' = \begin{cases} \sqrt[3]{\frac{b\tilde{\tau}_k}{c} \cdot \frac{4}{35}\,(C_\ell - \alpha\chi)} > 0 & \text{if } C_\ell > \alpha\chi \\ 0 & \text{if } C_\ell \leq \alpha\chi. \end{cases} \tag{B.14}$$

Appendix B.3.2. Non-positivity at critical value s'''

The function $\tilde{S}_2'$ yields the following non-positive value at the start point s''' of the convex area:

$$\tilde{S}_2'(s''') = \begin{cases} -0.11(C_\ell - \alpha\chi)^2\tilde{\tau}_k - 3cs'''^{\frac{2}{3}} < 0 & \text{if } C_\ell > \alpha\chi \\ 0 & \text{if } C_\ell \leq \alpha\chi. \end{cases} \tag{B.15}$$

Appendix B.3.3. Non-negativity in convex area

To find an argument s at which $\tilde{S}_2'$ is non-negative, we again distinguish the cases $C_\ell > \alpha\chi$ and $C_\ell \leq \alpha\chi$.

$C_\ell > \alpha\chi$. We consider the following function $\Psi^-(s)$, which constitutes a lower bound on $\tilde{S}_2'$, i.e., $\forall s > 0$. $\Psi^-(s) \leq \tilde{S}_2'(s)$:

$$\Psi^-(s) = \begin{cases} \frac{7c^2}{b\tilde{\tau}_k}s^6 - 4c\,(C_\ell - \alpha\chi)\,s^3 - 3cs^3 & \text{if } s \geq 1 \\ \frac{7c^2}{b\tilde{\tau}_k}s^6 - 4c\,(C_\ell - \alpha\chi)\,s^2 - 3cs^2 & \text{if } s < 1 \end{cases} \tag{B.16}$$

The highlights in Eq. (B.16) mark the differences of Ψ^- and $\tilde{S}_2'$ from Eq. (B.11).

The non-zero root of Ψ^- is $s^- = \max(\sqrt[3]{s_0}, \sqrt[4]{s_0})$, where

$$s_0 = \frac{b\tilde{\tau}_k}{c}\left(\frac{4}{7}\,(C_\ell - \alpha\chi) + \frac{3}{7}\right). \tag{B.17}$$

Since Ψ^- is a lower bound on $\tilde{S}_2'$, it holds that

$$\tilde{S}_2'(s^-) \geq \Psi^-(s^-) = 0. \tag{B.18}$$

The non-negativity point s^- is in the convex area if $s''' < s^-$, which demonstrably holds:

$$\begin{aligned} s''' &\overset{(B.14)}{=} \sqrt[3]{\frac{b\tilde{\tau}_k}{c}\cdot\frac{4}{35}\,(C_\ell - \alpha\chi)} < \sqrt[3]{\frac{b\tilde{\tau}_k}{c}\cdot\frac{4}{7}\,(C_\ell - \alpha\chi)} \\ &< \sqrt[3]{\frac{b\tilde{\tau}_k}{c}\left(\frac{4}{7}\,(C_\ell - \alpha\chi) + \frac{3}{7}\right)} \leq s^-. \end{aligned} \tag{B.19}$$

$C_\ell \leq \alpha\chi$. In this rare case, the lower bound function Ψ^- and its root s^- are more simply expressed:

$$\Psi^-(s) = \frac{7c^2}{b\tilde{\tau}_k}s^6 + 4c\,(C_\ell - \alpha\chi)\,s^2 - 3cs^{\mathbf{2}} \tag{B.20}$$

$$s^- = \sqrt[4]{\frac{b\tilde{\tau}_k}{c}\left(-\frac{4}{7}\,(C_\ell - \alpha\chi) + \frac{3}{7}\right)} \tag{B.21}$$

Again, the highlights in Eq. (B.20) mark the differences between Ψ^- and $\tilde{S}_2'$ from Eq. (B.11).

Note that Ψ^- is a *strict* lower bound (i.e., $\Psi^-(s) < \tilde{S}_2'(s)$) if $C_\ell < \alpha\chi$, and equals $\tilde{S}_2'$ for $C_\ell = \alpha\chi$. Hence, the following property holds on s^-:

$$\tilde{S}_2'(s^-)\begin{cases} > \Psi^-(s^-) & \text{if } C_\ell < \alpha\chi \\ = \Psi^-(s^-) & \text{if } C_\ell = \alpha\chi \end{cases} = 0 \tag{B.22}$$

The convex-area membership of $s^- > s'''$ is demonstrated analogously to the previous case:

$$s''' \overset{(B.14)}{=} 0 \overset{C_\ell \leq \alpha\chi}{<} \sqrt[4]{\frac{b\tilde{\tau}_k}{c}\left(-\frac{4}{7}\,(C_\ell - \alpha\chi) + \frac{3}{7}\right)} \overset{(B.21)}{=} s^-. \tag{B.23}$$

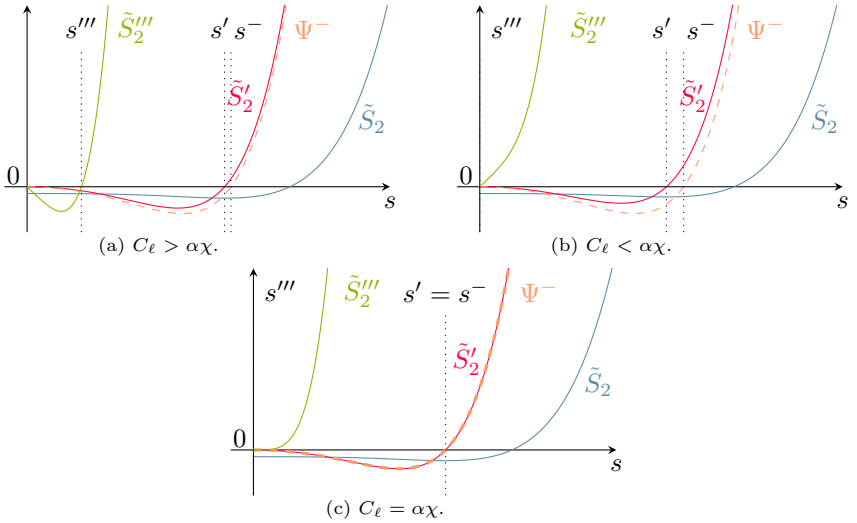

Figure B.17: Case distinction for determination of unique turning point in §Appendix B.3.4.

Appendix B.3.4. Combination of arguments

In summary, the function $\tilde{S}_2'$ evolves in a strictly convex fashion from $\tilde{S}_2'(s''') \leq 0$ at s''' to $\tilde{S}_2'(s^-) \geq 0$ at $s^- > s'''$. To demonstrate that these conditions imply a unique root with subsequent increasing behavior, we consider the relevant cases separately and visualize them in Fig. B.17 to simplify understanding:

$C_\ell > \alpha\chi$ (Fig. B.17a). In this case, we observe that $\tilde{S}_2'(s''') < 0$ (Eq. (B.15)) and $\tilde{S}_2'(s^-) \geq 0$ (Eq. (B.18)). Given this property, the function $\tilde{S}_2'$ has at least some increasing part between s''' and s^-, and at least the first root is in such an increasing part. Moreover, since $\tilde{S}_2'$ is strictly convex, the function keeps increasing once it is increasing, proving uniqueness of the root s' and increasing behavior after s'.

$C_\ell < \alpha\chi$ (Fig. B.17b). In this case, it holds that $\tilde{S}_2'(s''') = 0$ (Eq. (B.15)) and $\tilde{S}_2'(s^-) > 0$ (Eq. (B.22)). Strict convexity allows either (i) monotonic increase between $s''' = 0$ and $s^- > 0$, which creates a unique root at $s''' = 0$ such that $\tilde{S}_2'(s) > 0 \ \forall s > 0$, or (ii) a decrease followed by an increase, causing a unique root $s' \in (s''', s^-) = (0, s^-)$ above which $\tilde{S}_2'(s) > 0$.

$C_\ell = \alpha\chi$ (Fig. B.17c). In this last case, the function $\tilde{S}_2'$ has the property $\tilde{S}_2'(s''') = \tilde{S}_2'(s^-) = 0$ (Eqs. (B.15) and (B.22)). Given strict convexity, the function $\tilde{S}_2'$ can only return to 0 at s^- if it first decreases and then increases forever, causing a unique root $s' = s^-$ such that $\tilde{S}_2'(s) > 0 \ \forall s > s'$.

Appendix C. Proof of Theorem 2: Stability of the Short-Term Equilibrium

Our proof proceeds in three main steps, namely:

1. Stability investigation of the full linearized dynamics
2. Dimension reduction by characterization of the center manifold
3. Stability investigation of the lower-dimensional dynamics

Appendix C.1. Stability Investigation of the Full Linearized Dynamics

Appendix C.1.1. Centering the dynamics

Fundamentally, we consider the dynamic system $\dot{\boldsymbol{\sigma}} = f(\boldsymbol{\sigma})$, where the state variables are $\sigma = \left[\tilde{x}^{\text{btl}}, \tilde{w}^{\max}, \tilde{s}\right]^\top$, the adaptation function is $f = \left[\dot{x}^{\text{btl}}, \dot{w}^{\max}, \dot{s}\right]^\top$, and the equilibrium is $\tilde{\boldsymbol{\sigma}} = \left[\tilde{x}^{\text{btl}}, \tilde{w}^{\max}, \tilde{s}\right]^\top$, i.e., $\tilde{\boldsymbol{\sigma}} = f(\tilde{\boldsymbol{\sigma}})$. To show the asymptotic stability of the equilibrium $\tilde{\boldsymbol{\sigma}}$, we first center the dynamic system around the equilibrium: We transform the adaptation function f to f° such that $\tilde{\mathbf{z}} = \mathbf{0} = [0,0,0]^\top$ is an equilibrium of the dynamic system $\dot{\mathbf{z}} = f^\circ(\mathbf{z})$, i.e., $\mathbf{0} = \tilde{\mathbf{z}} = f^\circ(\tilde{\mathbf{z}})$. In our case, the dynamics in the differential equations for $\dot{x}^{\text{btl}}$, $\dot{w}^{\max}$ (Eq. (DE1)) and $\dot{s}$ (Eq. (DE2)) are centered as follows:

$$\dot{z}_1 = \frac{\alpha\left(z_1 + \tilde{x}^{\text{btl}}\right) C}{\alpha\left(z_1 + \tilde{x}^{\text{btl}}\right) + \frac{1}{\tilde{\tau}_k} W^\circ(z_2, z_3)} - \left(z_1 + \tilde{x}^{\text{btl}}\right) \tag{C.1}$$

$$\dot{z}_2 = \left(W^\circ(z_2, z_3) - (z_2 + \tilde{w}^{\max})\right) \cdot \frac{W^\circ(z_2, z_3)}{\tilde{\tau}_k} \cdot p^\circ(\mathbf{z}) \tag{C.2}$$

$$\dot{z}_3 = 1 - (z_3 + \tilde{s}) \cdot \frac{W^\circ(z_2, z_3)}{\tilde{\tau}_k} \cdot p^\circ(\mathbf{z}) \tag{C.3}$$

where both the CUBIC window-growth function W° and the loss-rate function p° are centered as well:

$$W^\circ(z_2, z_3) \overset{(1)}{=} (z_2 + \tilde{w}^{\max}) + c\left((z_3 + \tilde{s}) - \sqrt[3]{\frac{(z_2 + \tilde{w}^{\max})b}{c}}\right)^3 \tag{C.4}$$

$$p^\circ(\mathbf{z}) \overset{(4)}{=} \begin{cases} 1 - \frac{C_\ell}{\beta(z_1 + \tilde{x}^{\text{btl}}) + \frac{1}{\tilde{\tau}_k} W^\circ(z_2, z_3)} & \text{if } y_\ell(\mathbf{z}) > C_\ell \wedge q_\ell = B_\ell \\ 0 & \text{otherwise} \end{cases} \tag{C.5}$$

Appendix C.1.2. Linearizing the dynamics

We now linearize the adaptation function f° of this centered dynamic system around the equilibrium $\tilde{\mathbf{z}} = \mathbf{0}$ with the first-order Taylor expansion:

$$\mathcal{L}_{\mathbf{0}}[f^\circ](\mathbf{z}) = f^\circ(\mathbf{0}) + \mathbf{J}_{f^\circ}(\mathbf{0})\mathbf{z} = \mathbf{J}_{f^\circ}(\mathbf{0})\mathbf{z}, \tag{C.6}$$

where $\mathcal{L}_{\mathbf{0}}[f^\circ]$ indicates the linearization of the adaptation function f° around the new equilibrium $\mathbf{0}$, $\mathbf{J}_{f^\circ}(\mathbf{0})$ is the Jacobian matrix of f° evaluated at the equilibrium $\mathbf{0}$. Since $f^\circ(\mathbf{0}) = \mathbf{0}$, the dynamics around the equilibrium are dominated by $\mathbf{J}_{f^\circ}(\mathbf{0})\mathbf{z}$. The stability properties of the dynamic system thus depend on $\mathbf{J}_{f^\circ}(\mathbf{0})$, especially on its eigenvalues.

To find these eigenvalues, we need to characterize $\mathbf{J}_{f^\circ}(\mathbf{0})$, which is considerably simplified by the following identities:

$$\begin{aligned} &W^\circ(0,0) = \tilde{w}^{\max}, \qquad \frac{\partial W^\circ}{\partial z_2}(0,0) = 1, \\ &\frac{\partial W^\circ}{\partial z_3}(0,0) = 0, \quad \text{and} \quad \frac{\partial p^\circ}{\partial z_3}(\mathbf{0}) = 0. \end{aligned} \tag{C.7}$$

Moreover, we know the following properties of the equilibrium from §4:

$$\begin{aligned} &\tilde{s} > 0, \qquad \tilde{w}^{\max} = \frac{c}{b}\tilde{s}^3 > 0, \qquad p^\circ(\mathbf{0}) = \frac{b\tilde{\tau}_k}{c\tilde{s}^4} \in (0,1], \\ &\text{and} \quad \tilde{x}^{\text{btl}} = \max\left(\chi, C_\ell - \frac{1}{\alpha}\frac{\tilde{w}^{\max}}{\tilde{\tau}_k}\right) > 0. \end{aligned} \tag{C.8}$$

Using these equalities, $\mathbf{J}_{f^\circ}(\mathbf{0})$ in our case is:

$$\mathbf{J}_{f^\circ}(\mathbf{0}) = \begin{bmatrix} J_{11} & J_{12} & 0 \\ 0 & 0 & 0 \\ J_{31} & J_{32} & J_{33} \end{bmatrix} \tag{C.9}$$

$$\begin{aligned} J_{11} =& \frac{\alpha C_\ell \frac{1}{\tilde{\tau}_k} W^\circ(0,0)}{\left(\alpha \tilde{x}^{\mathrm{btl}} + \frac{1}{\tilde{\tau}_k} W^\circ(0,0)\right)^2} - 1 \\ =& \frac{\alpha C_\ell \frac{1}{\tilde{\tau}_k} \tilde{w}^{\max}}{\left(\alpha \tilde{x}^{\mathrm{btl}} + \frac{1}{\tilde{\tau}_k} \tilde{w}^{\max}\right)^2} - 1 < 0 \end{aligned} \tag{C.10}$$

$$\begin{aligned} J_{12} =& - \frac{\alpha C_\ell \tilde{x}^{\mathrm{btl}}}{\tilde{\tau}_k \left(\alpha \tilde{x}^{\mathrm{btl}} + \frac{1}{\tilde{\tau}_k} W^\circ(0,0)\right)^2} \cdot \frac{\partial W^\circ}{\partial z_2}(0,0) \\ =& - \frac{\alpha C_\ell \tilde{x}^{\mathrm{btl}}}{\tilde{\tau}_k \left(\alpha \tilde{x}^{\mathrm{btl}} + \frac{1}{\tilde{\tau}_k} \tilde{w}^{\max}\right)^2} < 0 \end{aligned} \tag{C.11}$$

$$\begin{aligned} J_{31} =& - \tilde{s} \frac{W^\circ(0,0)}{\tilde{\tau}_k} \frac{\beta C}{\left(\beta \tilde{x}^{\mathrm{btl}} + \frac{1}{\tilde{\tau}_k} W^\circ(0,0)\right)^2} \\ =& - \frac{\beta C_\ell \tilde{s} \tilde{w}^{\max}}{\tilde{\tau}_k \left(\beta \tilde{x}^{\mathrm{btl}} + \frac{1}{\tilde{\tau}_k} \tilde{w}^{\max}\right)^2} < 0 \end{aligned} \tag{C.12}$$

$$\begin{aligned} J_{32} =& - \frac{\tilde{s}}{\tilde{\tau}_k} \cdot \frac{\partial W^\circ}{\partial z_2}(0,0) \cdot \left(1 - \frac{C_\ell}{\beta \tilde{x}^{\mathrm{btl}} + \frac{1}{\tilde{\tau}_k} W^\circ(0,0)}\right) \\ & - \tilde{s} \cdot \frac{W^\circ(0,0)}{\tilde{\tau}_k} \cdot \frac{C_\ell}{\tilde{\tau}_k (\beta \tilde{x}^{\mathrm{btl}} + \frac{1}{\tilde{\tau}_k} W^\circ(0,0))^2} \cdot \frac{\partial W^\circ}{\partial z_2}(0,0) \\ =& - \frac{\tilde{s}}{\tilde{\tau}_k} \cdot p^\circ(\mathbf{0}) - \frac{\tilde{s} \tilde{w}^{\max}}{\tilde{\tau}_k^2} \frac{C_\ell}{\left(\beta \tilde{x}^{\mathrm{btl}} + \frac{1}{\tilde{\tau}_k} \tilde{w}^{\max}\right)^2} < 0 \end{aligned} \tag{C.13}$$

$$\begin{aligned} J_{33} =& - \frac{W^\circ(0,0)}{\tilde{\tau}_k} \cdot p^\circ(\mathbf{0}) - \frac{\tilde{s}}{\tilde{\tau}_k} \cdot \frac{\partial W^\circ}{\partial z_3}(0,0) \cdot p^\circ(\mathbf{0}) \\ & - \tilde{s} \cdot \frac{W^\circ(0,0)}{\tilde{\tau}_k} \cdot \frac{\partial p^\circ}{\partial z_3}(\mathbf{0}) \\ =& - \frac{1}{\tilde{s}} < 0 \end{aligned} \tag{C.14}$$

Hence, all entries of $\mathbf{J}_{f^\circ}(\mathbf{0})$ are negative. Among the above matrix entries, the bounding of the entry J_{11} in Eq. (C.10) is not trivial and requires a case distinction on χ:

$\chi \leq C_\ell - \tilde{w}^{\max}/(\alpha \tilde{\tau}_k)$. In this case, the bounding is straightforward:

$$\tilde{x}^{\mathrm{btl}} \overset{\text{(C.8)}}{=} \max\left(\chi, C_\ell - \frac{\tilde{w}^{\max}}{\alpha \tilde{\tau}_k}\right) \overset{\text{Case}}{=} C_\ell - \frac{\tilde{w}^{\max}}{\alpha \tilde{\tau}_k} \tag{C.15}$$

$$\implies \alpha \tilde{x}^{\mathrm{btl}} + \frac{\tilde{w}^{\max}}{\tilde{\tau}_k} = \alpha C_\ell \implies \tag{C.16}$$

$$J_{11} = \frac{\alpha C_\ell \frac{\tilde{w}^{\max}}{\tilde{\tau}_k}}{(\alpha C_\ell)^2} - 1 = \frac{\frac{\tilde{w}^{\max}}{\tilde{\tau}_k}}{\alpha C_\ell} - 1 \leq \frac{\alpha(C_\ell - \chi)}{\alpha C_\ell} - 1 < 0 \tag{C.17}$$

$\chi > C_\ell - \tilde{w}^{\max}/(\alpha\tilde{\tau}_k)$. For this case, we note that $\tilde{x}^{\text{btl}}$ is at the minimum χ of its domain:

$$\tilde{x}^{\text{btl}} \overset{(C.8)}{=} \max\left(\chi, C_\ell - \frac{\tilde{w}^{\max}}{\alpha\tilde{\tau}_k}\right) = \chi \tag{C.18}$$

Moreover, we obtain a lower bound on the CUBIC equilibrium rate $\tilde{x}^{\text{C}}$ for this case:

$$\chi > C_\ell - \frac{\tilde{w}^{\max}}{\alpha\tilde{\tau}_k} \iff \tilde{x}^{\text{C}} = \frac{\tilde{w}^{\max}}{\tilde{\tau}_k} > \alpha\left(C_\ell - \chi\right). \tag{C.19}$$

Moreover, we obtain another lower bound $\hat{x}^{\text{C}}$ on the CUBIC equilibrium rates that lead to a negative Jacobian entry J_{11}:

$$J_{11}\left(\tilde{x}^{\text{C}}\right) \overset{(C.10)}{=} \frac{\alpha C_\ell \tilde{x}^{\text{C}}}{\left(\alpha\chi + \tilde{x}^{\text{C}}\right)^2} - 1 < 0 \tag{C.20}$$

$$\iff \tilde{x}^{\text{C}2} + \alpha(2\chi - C_\ell)\tilde{x}^{\text{C}} + \alpha^2\chi^2 =: \Psi(\tilde{x}^{\text{C}}) > 0 \tag{C.21}$$

$$\iff \tilde{x}^{\text{C}} > \alpha\frac{\sqrt{C_\ell\left(C_\ell - 4\chi\right)} + (C_\ell - 2\chi)}{2} =: \hat{x}^{\text{C}}. \tag{C.22}$$

We note that the lower bound $\hat{x}^{\text{C}}$ in Eq. (C.22) only exists if $4\chi \leq C_\ell$. In contrast, the non-existence of $\hat{x}^{\text{C}}$ means that Ψ from Eq. (C.21) has no root. Since Ψ is strictly convex, and a strictly convex function with no roots is always positive, $\Psi > 0$ from Eq. (C.21) holds for all $\tilde{x}^{\text{C}}$.

Conversely, if $4\chi \leq C_\ell$ and $\hat{x}^{\text{C}}$ therefore exists, we need to verify that $\hat{x}^{\text{C}} \leq \alpha(C_\ell - \chi)$ such that all $\tilde{x}^{\text{C}} > \alpha(C_\ell - \chi)$ (i.e., all CUBIC equilibrium rates possible according to Eq. (C.19)) lead to a negative J_{11}. Given $\hat{x}^{\text{C}}$ from Eq. (C.22), we obtain:

$$\begin{aligned}&\alpha\frac{\sqrt{C_\ell\left(C_\ell - 4\chi\right)} + (C_\ell - 2\chi)}{2} \leq \alpha(C_\ell - \chi) \iff \\ &-4\chi C_\ell \leq 0 \iff \chi \geq 0 \iff \top.\end{aligned} \tag{C.23}$$

In summary, $J_{11} < 0$ thus holds for all $\tilde{w}^{\max}/\tilde{\tau}_k$ and all χ.

Appendix C.1.3. Finding the eigenpairs

Finding the eigenvalues and eigenvectors of $\mathbf{J}_{f^\circ}(\mathbf{0})$ means finding $(\lambda, \mathbf{v})$ such that $\lambda \in \mathbb{C}$ is an eigenvalue, $\mathbf{v} \in \mathbb{C}^3$ is the corresponding eigenvector and must be non-zero ($\mathbf{v} \neq \mathbf{0}$), and $\mathbf{J}_{f^\circ}(\mathbf{0})\mathbf{v} = \lambda\mathbf{v}$. Hence, any solution $(\lambda, \mathbf{v})$ satisfies the following system of equations:

$$(J_{11} - \lambda)v_1 + J_{12}v_2 = 0 \tag{C.24}$$

$$\lambda v_2 = 0 \tag{C.25}$$

$$J_{31}v_1 + J_{32}v_2 + (J_{33} - \lambda)v_3 = 0 \tag{C.26}$$

Eq. (C.25) implies that λ or v_2 must be zero.

$\lambda = 0$. First, we check whether $\lambda = 0$ is an eigenvalue of $\mathbf{J}_{f^\circ}(\mathbf{0})$. Assuming $\lambda = 0$, the equation system reduces to two equations:

$$J_{11}v_1 + J_{12}v_2 = 0 \qquad J_{31}v_1 + J_{32}v_2 + J_{33}v_3 = 0 \tag{C.27}$$

Given this equation system, we can identify the following eigenvector $v^{(1)}$ for the eigenvalue $\lambda^{(1)} = 0$:

$$v_1^{(1)} \in \mathbb{C} \setminus \{0\} \qquad v_2^{(1)} = -\frac{J_{11}}{J_{12}}v_1^{(1)} \qquad v_3^{(1)} = \frac{J_{11}J_{32} - J_{12}J_{31}}{J_{12}J_{33}}v_1^{(1)} \tag{C.28}$$

This eigenvector exists because the denominators are non-zero given $J_{12} < 0$ and $J_{12}J_{33} > 0$. Moreover, $J_{11} > 0$ ensures a non-zero eigenvector.

$v_2 = 0$. To find further eigenvalues, we now assume $v_2 = 0$, leading again to a reduced equation system:

$$(J_{11} - \lambda)v_1 = 0 \qquad J_{31}v_1 + (J_{33} - \lambda)v_3 = 0 \tag{C.29}$$

For this equation system, we can perform a case distinction on v_1, the first entry of the eigenvector:

- $\boldsymbol{v_1 \neq 0}$ **:** Assuming $v_1 \neq 0$ yields the eigenpair $(\lambda^{(2)}, \mathbf{v}^{(2)})$:

$$\begin{aligned} \lambda^{(2)} = J_{11} \qquad & v_1^{(2)} \in \mathbb{C} \setminus \{0\} \\ v_2^{(2)} = 0 \qquad & v_3^{(2)} = \frac{J_{31}}{J_{11} - J_{33}} v_1^{(2)} \end{aligned} \tag{C.30}$$

- $\boldsymbol{v_1 = 0}$ **:** In this case, the equation system collapses to the single equation $(J_{33} - \lambda)v_3 = 0$, where $v_3 \neq 0$ because not all entries of an eigenvector can be 0. Hence, $\mathbf{J}_{f^\circ}(\mathbf{0})$ has the following eigenpair $(\lambda^{(3)}, \mathbf{v}^{(3)})$:

$$\begin{aligned} \lambda^{(3)} = J_{33} \overset{(C.14)}{=} -\frac{1}{\tilde{s}} \overset{(C.8)}{<} 0 \qquad & v_1^{(3)} = 0 \\ v_2^{(3)} = 0 \qquad & v_3^{(3)} \in \mathbb{C} \setminus \{0\} \end{aligned} \tag{C.31}$$

Summary of eigenpairs. The Jacobian matrix $\mathbf{J}_{f^\circ}(\mathbf{0})$ thus has zero and negative eigenvalues. For convenience, we categorize the eigenvectors into sets corresponding to zero and negative eigenvalues, respectively:

$$V^0 = \{\mathbf{v}^{(1)}\} \qquad V^- = \{\mathbf{v}^{(2)}, \mathbf{v}^{(3)}\} \tag{C.32}$$

The presence of both zero and negative eigenvalues means that the stability properties of the original nonlinear dynamic system $\dot{\mathbf{z}} = f^\circ(\mathbf{z})$ cannot be derived from the linearized system $\dot{\mathbf{z}} = \mathbf{J}_{f^\circ}(\mathbf{0})\mathbf{z}$ [48]. Instead, higher-order terms determine the stability.

Appendix C.2. Dimension Reduction via the Center Manifold

While the linearized system is inconclusive about the desired stability properties, it allows some insight into the dynamics of the nonlinear system when using center-manifold theory.

Appendix C.2.1. Center-manifold properties

To introduce the center manifold, we note that the subspace spanned by the eigenvectors in V^- is the *stable subspace* of the Jacobian $\mathbf{J}_{f^\circ}(\mathbf{0})$, and the subspace spanned by the eigenvectors in V^0 is the *center subspace* [51]. Each of these subspaces is associated with a manifold that has the same dimension as the corresponding subspace, and is tangential to the corresponding subspace at the equilibrium [17].

Since our system has only has a stable manifold and a center manifold (and no unstable manifold, which would be associated with positive eigenvalues), we can use the *center-manifold emergence theorem* [21]. This theorem states that given a starting point sufficiently close to the center manifold, the dynamics converge exponentially quickly to the center manifold, and thus approach a trajectory on the center manifold. The overall dynamics of the nonlinear system can thus be approximated by the dynamics on the center manifold, which have lower dimension and thus allow a more tractable analysis.

Appendix C.2.2. Center-manifold dynamics

To derive the dynamics on the center manifold, we start by decoupling the system state $\mathbf{z}$ along subspaces, i.e., we transform it onto a different basis such that every variable only effects a change along either the center or the stable subspace. We achieve this by a coordinate transformation using the eigenbasis:

$$\begin{aligned} \mathbf{z} = \mathbf{T}\boldsymbol{\zeta} = [\mathbf{v}^{(1)}\ \mathbf{v}^{(2)}\ \mathbf{v}^{(3)}]\boldsymbol{\zeta} = \begin{bmatrix} T_{11} & T_{12} & 0 \\ T_{21} & 0 & 0 \\ T_{31} & T_{32} & T_{33} \end{bmatrix} \begin{bmatrix} \zeta_1 \\ \zeta_2 \\ \zeta_3 \end{bmatrix} \\ \iff \boldsymbol{\zeta} = \mathbf{T}^{-1}\mathbf{z}, \end{aligned} \tag{C.33}$$

where ζ_1 is the variable associated with the center subspace, and ζ_2 and ζ_3 are the variables associated with the stable subspace. From the structure of $\mathbf{T}$, we see that the center variable ζ_1 can be expressed exclusively by z_2 (corresponding to $w^{\max}$):

$$z_2 = T_{21}\zeta_1 \quad \Longleftrightarrow \quad \zeta_1 = \frac{z_2}{T_{21}}. \tag{C.34}$$

According to the center-manifold existence theorem, a manifold Γ_c exists with the following properties around the equilibrium [51]:

$$\begin{aligned}\Gamma_c = \{(\zeta_1,\zeta_2,\zeta_3) \ \mid \zeta_2 = h_2(\zeta_1),\ h_2(0)=0,\ {h_2}'(0)=0,\\ \zeta_3 = h_3(\zeta_1),\ h_3(0)=0,\ {h_3}'(0)=0\}\end{aligned} \tag{C.35}$$

where both h_2 and h_3 are one-dimensional functions of the form:

$$h(\zeta_1) = \sum_{i=2}^{\infty} a_i \zeta_1^i. \tag{C.36}$$

Intuitively, in our case, the center manifold Γ_c corresponds to a curve in three-dimensional space, which is tangential to the center subspace at the equilibrium $\mathbf{0}$ and is fully describable by the center variable ζ_1. The overall dynamics of the nonlinear system move along that curve, although it is not clear yet whether towards or away from the equilibrium. To identify this direction, we only need to consider the following one-dimensional dynamics along the center manifold:

$$\dot{\zeta}_1 \overset{(C.34)}{=} \frac{1}{T_{21}}\dot{z}_2(\mathbf{z}) \overset{(C.33)}{=} \frac{1}{T_{21}}\dot{z}_2(\mathbf{T}\boldsymbol{\zeta}') \tag{C.37}$$

where

$$\boldsymbol{\zeta}' \overset{(C.35)}{=} \begin{bmatrix}\zeta_1\\ h_2(\zeta_1)\\ h_3(\zeta_1)\end{bmatrix} \overset{(C.34)}{=} \begin{bmatrix}z_2/T_{21}\\ h_2(z_2/T_{21})\\ h_3(z_2/T_{21})\end{bmatrix}. \tag{C.38}$$

Appendix C.3. Stability Investigation of the Lower-Dimensional Dynamics

So far, we have reduced the full dynamics to the lower-dimensional center-manifold dynamics, which we can now investigate.

Appendix C.3.1. Taylor expansion of center-manifold dynamics

The one-dimensional center-manifold dynamics in Eq. (C.37) suggests that the dynamics $\dot{z}_2$ from Eq. (C.2) are solely relevant for stability. However, since we investigate these dynamics on the center manifold, the state variables in $\mathbf{z}$ need to be expressed based on the center-manifold functions of z_2:

$$\hat{\mathbf{z}}(z_2) = \mathbf{T}\boldsymbol{\zeta}' \overset{\substack{(C.33)\\(C.38)}}{=} \begin{bmatrix} T_{11}\frac{z_2}{T_{21}} + T_{12}h_2\left(\frac{z_2}{T_{21}}\right)\\ z_2\\ T_{31}\frac{z_2}{T_{21}} + T_{32}h_2\left(\frac{z_2}{T_{21}}\right) + T_{33}h_3\left(\frac{z_2}{T_{21}}\right)\end{bmatrix}. \tag{C.39}$$

Hence, $\dot{z}_2$ with the variables from $\mathbf{z}$ substituted by $\hat{\mathbf{z}}$ is:

$$\begin{aligned}\dot{z}_2 = &(W^{\circ}(z_2,\hat{z}_3(z_2)) - (z_2 + \tilde{w}^{\max}))\cdot\\ &\frac{W^{\circ}(z_2,\hat{z}_3(z_2))}{\tilde{\tau}_k}\cdot p^{\circ}(\hat{\mathbf{z}}(z_2)).\end{aligned} \tag{C.40}$$

Around the equilibrium $\tilde{z}_2 = 0$, this evolution function $\dot{z}_2$ can be approximated via a Taylor expansion of third degree:

$$\dot{z}_2(z_2') \approx \dot{z}_2(0) + \frac{\partial \dot{z}_2}{\partial z_2}(0)\cdot z_2' + \frac{\partial^2 \dot{z}_2}{\partial z_2^2}(0)\cdot\frac{{z_2'}^2}{2!} + \frac{\partial^3 \dot{z}_2}{\partial z_2^3}(0)\cdot\frac{{z_2'}^3}{3!}. \tag{C.41}$$

By using the Symbolic Math Toolbox of Matlab [33], this approximated function can be reduced to the following expression:

$$\dot{z}_2(z_2') \approx \frac{c\tilde{w}^{\max} T_{31}^3 p^\circ(\mathbf{0})}{\tilde{\tau}_k T_{21}^3} \cdot {z_2'}^3 = K {z_2'}^3. \tag{C.42}$$

It is easy to see that asymptotic stability of this system requires a negative K: If $z_2' < 0$ (below the equilibrium), z_2' would be positively affected (multiplication of negative numbers) and thus drawn closer to the equilibrium at 0, whereas if $z_2' > 0$, z_2' would be negatively affected, and thereby also attracted to the equilibrium at 0. To prove asymptotic stability, we thus have to show:

$$\begin{aligned} K < 0 &\overset{(C.42)}{\iff} \frac{c\tilde{w}^{\max} T_{31}^3 p^\circ(\mathbf{0})}{\tilde{\tau}_k T_{21}^3} < 0 \\ &\overset{(C.33)}{\iff} \frac{c\tilde{w}^{\max} {v_3^{(1)}}^3 p^\circ(\mathbf{0})}{\tilde{\tau}_k {v_2^{(1)}}^3} < 0 \end{aligned} \tag{C.43}$$

where $\mathbf{v}^{(1)}$ fulfills the condition in Eq. (C.28).

Without loss of generality, we set $v_1^{(1)} < 0$, which implies (together with $J_{11} < 0$ and $J_{12} < 0$):

$$v_2^{(1)} \overset{(C.28)}{=} -\frac{J_{11}}{J_{12}} v_1^{(1)} > 0. \tag{C.44}$$

Since c, $\tilde{w}^{\max}$, $p^\circ(\mathbf{0})$, and $\tilde{\tau}_k$ are all known to be positive, asymptotic stability depends on the following condition:

$$\begin{aligned} &{v_3^{(1)}}^3 < 0 \iff v_3^{(1)} < 0 \overset{(C.28)}{\iff} \\ &\frac{J_{11}J_{32} - J_{12}J_{31}}{J_{12}J_{33}} v_1^{(1)} < 0 \iff \frac{J_{11}J_{32} - J_{12}J_{31}}{J_{12}J_{33}} > 0. \end{aligned} \tag{C.45}$$

Since $J_{12} < 0$ and $J_{33} < 0$, we can simplify this condition even further to:

$$J_{11}J_{32} > J_{12}J_{31} \quad \iff \quad J_{11} < \frac{J_{31}}{J_{32}} J_{12}. \tag{C.46}$$

To check whether this condition holds, we again perform a case distinction regarding χ, i.e., we distinguish the cases $\chi \leq C_\ell - \tilde{w}^{\max}/(\alpha\tilde{\tau}_k)$ and $\chi > C_\ell - \tilde{w}^{\max}/(\alpha\tilde{\tau}_k)$.

Appendix C.3.2. $\chi \leq C_\ell - \tilde{w}^{\max}/(\alpha\tilde{\tau}_k)$

In this case, the expanded form of Eq. (C.46) can be simplified by the finding in Eq. (C.16):

$$\begin{aligned} J_{11} &\overset{(C.10)}{=} \frac{\alpha C_\ell}{\tilde{\tau}_k\left(\alpha\tilde{x}^{\text{btl}} + \frac{1}{\tilde{\tau}_k}\tilde{w}^{\max}\right)^2}\cdot\tilde{w}^{\max} - 1 \overset{(C.46)}{<} \\ &- \frac{J_{31}}{J_{32}}\frac{\alpha C_\ell}{\tilde{\tau}_k\left(\alpha\tilde{x}^{\text{btl}} + \frac{1}{\tilde{\tau}_k}\tilde{w}^{\max}\right)^2}\cdot\tilde{x}^{\text{btl}} \overset{(C.11)}{=} \frac{J_{31}}{J_{32}}J_{12} \end{aligned} \tag{C.47}$$

$$\overset{(C.16)}{\iff} \frac{1}{\tilde{\tau}_k\alpha C_\ell}\cdot\tilde{w}^{\max} - 1 < -\frac{J_{31}}{J_{32}}\frac{1}{\tilde{\tau}_k\alpha C_\ell}\cdot\tilde{x}^{\text{btl}} \tag{C.48}$$

$$\overset{\substack{\cdot\tilde{\tau}_k\alpha C_\ell \\ /\tilde{x}^{\text{btl}}}}{\iff} (\tilde{w}^{\max} - \tilde{\tau}_k\alpha C_\ell)\cdot\frac{1}{\tilde{x}^{\text{btl}}} < -\frac{J_{31}}{J_{32}} \tag{C.49}$$

$$\overset{(C.15)}{\iff} (\tilde{w}^{\max} - \tilde{\tau}_k\alpha C_\ell)\cdot\frac{1}{C_\ell - \frac{\tilde{w}^{\max}}{\tilde{\tau}_k\alpha}} < -\frac{J_{31}}{J_{32}} \tag{C.50}$$

$$\overset{\text{expand}}{\iff} (\tilde{w}^{\max} - \tilde{\tau}_k\alpha C_\ell)\cdot\frac{\tilde{\tau}_k\alpha}{\tilde{\tau}_k\alpha C_\ell - \tilde{w}^{\max}} < -\frac{J_{31}}{J_{32}} \tag{C.51}$$

$$\overset{\substack{\text{cancel} \\ \cdot -1}}{\iff} \tilde{\tau}_k\alpha > \frac{J_{31}}{J_{32}} \overset{1/\cdot}{\iff} \frac{J_{32}}{J_{31}} > \frac{1}{\tilde{\tau}_k\alpha}. \tag{C.52}$$

In turn, expanding the ratio J_{32}/J_{31} yields:

$$\begin{aligned} \frac{J_{32}}{J_{31}} &\overset{\substack{(C.13) \\ (C.12)}}{=} -\left(\frac{\tilde{s}}{\tilde{\tau}_k}\cdot p^\circ(\mathbf{0}) + \frac{\tilde{s}\tilde{w}^{\max}}{\tilde{\tau}_k^2}\frac{C_\ell}{\left(\beta\tilde{x}^{\text{btl}} + \frac{1}{\tilde{\tau}_k}\tilde{w}^{\max}\right)^2}\right)\cdot \\ &\left(-\frac{\tilde{\tau}_k\left(\beta\tilde{x}^{\text{btl}} + \frac{1}{\tilde{\tau}_k}\tilde{w}^{\max}\right)^2}{\beta C_\ell\tilde{s}\tilde{w}^{\max}}\right) \end{aligned} \tag{C.53}$$

$$= \frac{p^\circ(\mathbf{0})\left(\beta\tilde{x}^{\text{btl}} + \frac{1}{\tilde{\tau}_k}\tilde{w}^{\max}\right)^2}{\beta C_\ell\tilde{w}^{\max}} + \frac{1}{\tilde{\tau}_k\beta} > \frac{1}{\tilde{\tau}_k\alpha}. \tag{C.54}$$

The bound holds because $\beta \leq \alpha$ and the first term on the LHS in Eq. (C.54) is strictly positive. Hence, also Eq. (C.46) holds.

Appendix C.3.3. $\chi > C_\ell - \tilde{w}^{\max}/(\alpha\tilde{\tau}_k)$

In this case, $\tilde{x}^{\text{btl}} \overset{(C.18)}{=} \chi$ and the expanded form of Eq. (C.46) is thus:

$$\frac{\alpha C_\ell}{\tilde{\tau}_k\left(\alpha\chi + \frac{1}{\tilde{\tau}_k}\tilde{w}^{\max}\right)^2}\cdot\tilde{w}^{\max} - 1 \overset{(C.46)}{<} -\frac{J_{31}}{J_{32}}\frac{\alpha C_\ell\chi}{\tilde{\tau}_k\left(\alpha\chi + \frac{1}{\tilde{\tau}_k}\tilde{w}^{\max}\right)^2} \tag{C.55}$$

$$\iff \frac{J_{32}}{J_{31}} > \frac{\alpha C_\ell\tilde{\tau}_k\chi}{\tilde{w}^{\max\,2} + \alpha(2\chi - C_\ell)\tilde{\tau}_k\tilde{w}^{\max} + \alpha^2 C_\ell^2\chi^2} \tag{C.56}$$

Expanding the ratio J_{32}/J_{31} yields:

$$\begin{aligned}\frac{J_{32}}{J_{31}} \overset{\text{(C.13)}}{\underset{\text{(C.12)}}{=}} &- \left(\frac{\tilde{s}}{\tilde{\tau}_k} \cdot p^\circ(\mathbf{0}) + \frac{\tilde{s}\tilde{w}^{\max}}{\tilde{\tau}_k^2} \frac{C_\ell}{\left(\beta\chi + \frac{1}{\tilde{\tau}_k}\tilde{w}^{\max}\right)^2} \right) \cdot \\ &\left(-\frac{\tilde{\tau}_k \left(\beta\chi + \frac{1}{\tilde{\tau}_k}\tilde{w}^{\max}\right)^2}{\beta C_\ell \tilde{s} \tilde{w}^{\max}} \right) \\ = &\frac{\tilde{\tau}_k \left(\beta\chi + \frac{\tilde{w}^{\max}}{\tilde{\tau}_k}\right)^2}{\beta C_\ell \tilde{s} \tilde{w}^{\max\,2}} + \frac{1}{\beta\tilde{\tau}_k} > \frac{1}{\beta\tilde{\tau}_k}. \end{aligned} \tag{C.57}$$

Thanks to this neat lower bound of J_{32}/J_{31}, Eq. (C.56) is implied by the following stronger condition:

$$\begin{aligned}\frac{J_{32}}{J_{31}} &\overset{\text{(C.57)}}{>} \frac{1}{\beta\tilde{\tau}_k} > \frac{\alpha C_\ell \tilde{\tau}_k \chi}{\tilde{w}^{\max\,2} + \alpha(2\chi - C_\ell)\tilde{\tau}_k \tilde{w}^{\max} + \alpha^2 C_\ell^2 \chi^2} && \text{(C.58)} \\ &\iff \frac{1}{\beta\tilde{\tau}_k}\tilde{w}^{\max\,2} + \frac{\alpha\,(2\chi - C)}{\beta}\tilde{w}^{\max} + \frac{\tilde{\tau}_k \alpha^2 \chi^2}{\beta} - \tilde{\tau}_k \alpha C_\ell \chi \\ &=: \Psi(\tilde{w}^{\max}) > 0. && \text{(C.59)}\end{aligned}$$

To verify Eq. (C.59) for all $\tilde{w}^{\max} > \tilde{\tau}_k\alpha(C_\ell - \chi)$, we first note that Ψ is convex. Hence, if Ψ has no roots, the convexity of Ψ implies that $\Psi(\tilde{w}^{\max}) > 0$ holds for any $\tilde{w}^{\max}$. In contrast, if Ψ has roots, $\Psi(\tilde{w}^{\max}) > 0$ holds for any $\tilde{w}^{\max}$ above the upper root ψ of Ψ, which is:

$$\psi = \frac{\tilde{\tau}_k}{2}\left(\alpha\,(C_\ell - 2\chi) + \sqrt{\alpha^2 C_\ell^2 + 4\alpha C_\ell\,(\beta - \alpha)\,\chi}\right) \tag{C.60}$$

The truth of $\Psi(\tilde{w}^{\max}) > 0\ \forall \tilde{w}^{\max} > \tilde{\tau}_k\alpha(C_\ell - \chi)$ is confirmed by the fact that ψ is below the relevant area of argument $\tilde{w}^{\max}$:

$$\begin{aligned}&\psi \leq \tilde{\tau}_k\alpha(C_\ell - \chi) \overset{\cdot 2/\tilde{\tau}_k}{\iff} \\ &\alpha\,(C_\ell - 2\chi) + \sqrt{\alpha^2 C_\ell^2 + 4\alpha C_\ell\,(\beta - \alpha)\,\chi} \leq 2\alpha(C_\ell - \chi) \\ &\overset{-\alpha(C_\ell - 2\chi)}{\iff} \sqrt{\alpha^2 C_\ell^2 + 4\alpha C_\ell\,(\beta - \alpha)\,\chi} \leq \alpha C_\ell \\ &\overset{(\cdot)^2}{\underset{-\alpha C_\ell}{\iff}} 4\alpha C_\ell(\beta - \alpha)\chi \leq 0 \overset{\substack{\beta \leq \alpha \\ \chi > 0}}{\iff} \top.\end{aligned} \tag{C.61}$$

Appendix C.3.4. Conclusion

In conclusion, the relation between the Jacobian entries J_{11}, J_{12}, J_{31}, and J_{32} as given in Eq. (C.46) ensures a negative third entry $v_3^{(1)}$ in the center eigenvector, which is required for a negative coefficient in the third-order Taylor expansion of the center-manifold dynamics in Eq. (C.43). The negativity of this coefficient guarantees asymptotic stability of the center-manifold dynamics in Eq. (C.40), and thus of the full dynamic system.

Appendix D. Proof of Theorem 3: BBR-CUBIC Oscillation

Appendix D.1. Update Functions

We start the proof by characterizing the update function $w^{\leftarrow}$ and used in the discrete-time process in Eq. (21). Conceptually, this function $w^{\leftarrow}(w)$ yields the CUBIC window size after an interval of the short-term dynamics given BBR probing strength α, which in turn results from CUBIC window size w at the beginning of the interval. We denote this resulting probing strength by $\alpha^{\leftarrow}(w)$, and characterize it in §Appendix D.1.1 before characterizing $w^{\leftarrow}$ in §Appendix D.1.2.

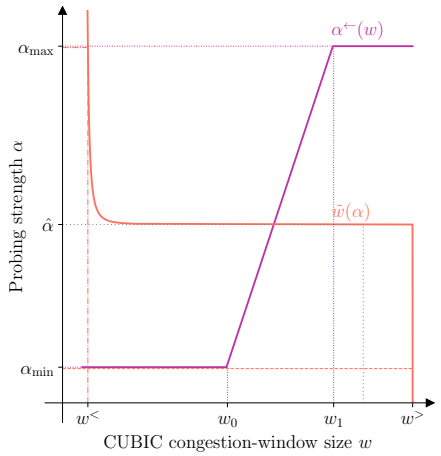

Figure D.18: Illustration of functions $\alpha^{\leftarrow}(w)$ and $\tilde{w}(\alpha)$.

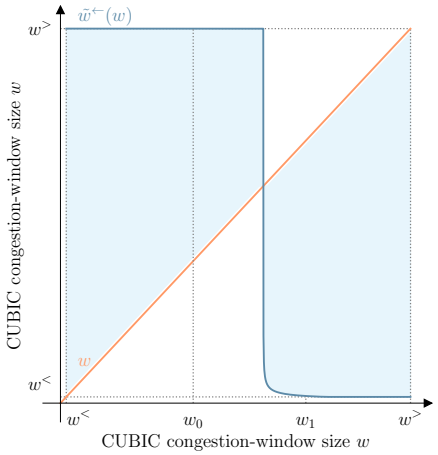

Figure D.19: Illustration of function $\tilde{w}^{\leftarrow}(w)$, and value range for function $w^{\leftarrow}(w)$.

Appendix D.1.1. α-update function $\alpha^{\leftarrow}$

From Eq. (15) in the fluid-equilibrium model in §4, we know that α is determined based on the queue length q_ℓ^- that remains when the BBR flow backs off:

$$\alpha^{\leftarrow}(w) = \min(5/4, \dot{\alpha}^{\leftarrow}(w)) \tag{D.1}$$

$$\text{where} \quad \dot{\alpha}^{\leftarrow}(w) = \frac{2}{\tau_i}\left(\tau_i^{\mathrm{p}} + \frac{q_\ell^-(w)}{C_\ell}\right) \tag{D.2}$$

$$= \frac{2}{\tau_i}\left(\tau_i^{\mathrm{p}} + \frac{[4 + (1-b)w - \tau_\ell^{\mathrm{p}} C_\ell]_0^{B_\ell}}{C_\ell}\right). \tag{D.3}$$

This function $\alpha^{\leftarrow}(w)$ achieves its minimum value $\alpha_{\min}$ if $q_\ell^- = 0$, which is achieved for all CUBIC window sizes $w \leq w_0$, where:

$$w_0 = \frac{1}{1-b}\left(C_\ell \tau_\ell^{\mathrm{p}} - 4\right) \implies \alpha_{\min} = \alpha^{\leftarrow}(w_0) = \frac{2\tau_i^{\mathrm{p}}}{\tau_i} \tag{D.4}$$

Conversely, the maximum $\alpha_{\max}$ is not achieved for $q_\ell^- = B_\ell$, as in this case $\dot{\alpha}^{\leftarrow} = 2\tau_i/\tau_i = 2$. Instead, the maximum value $\alpha_{\max}$ is achieved for all window sizes $w \geq w_1$, where

$$w_1 = \frac{1}{1-b}\left(C_\ell\left(\frac{5}{8}\tau_i + \tau_\ell^{\mathrm{p}} - \tau_i^{\mathrm{p}}\right) - 4\right) \implies \dot{\alpha}^{\leftarrow}(w_1) = 5/4$$
$$\implies \alpha^{\leftarrow}(w_1) = 5/4 = \alpha_{\max}. \tag{D.5}$$

Given the above value range, we rewrite the function $\alpha^{\leftarrow}$ such that its constant and linear pieces become obvious:

$$\alpha^{\leftarrow}(w) = \begin{cases} \alpha_{\min} = \frac{2\tau_i^{\mathrm{p}}}{\tau_i} & \text{if } w \leq w_0, \\ \dot{\alpha}(w) = \frac{2}{\tau_i}\left(\tau_i^{\mathrm{p}} + \frac{w+4-\tau_\ell^{\mathrm{p}} C_\ell}{C_\ell}\right) & \text{if } w \in (w_0, w_1), \\ \alpha_{\max} = 5/4 & \text{if } w \geq w_1. \end{cases} \tag{D.6}$$

This function $\alpha^{\leftarrow}$ is illustrated in Fig. D.18.

Appendix D.1.2. Window-update function $w^{\leftarrow}$

The window-update function $w^{\leftarrow}(w)$ yields the CUBIC window size after an interval with initial window size w and corresponding BBR probing strength $\alpha = \alpha^{\leftarrow}(w)$. Since this new CUBIC window size is the

result of convergence towards the short-term equilibrium window size $\tilde{w}(\alpha)$, we first revisit $\tilde{w}(\alpha)$ based on Theorem 1. While this function does not have a closed-form representation, we can still conclude that $\tilde{w}(\alpha)$ has a two-part structure. In particular, we know that an inflection point $\hat{\alpha} > 1$ exists such that $\tilde{w}(\alpha)$ is found by solving the equation $\tilde{S}_2(s) = 0$ (cf. Eq. (20)) for all $\alpha < \hat{\alpha}$, and and found by solving $\tilde{S}_1(s) = 0$ (cf. Eq. (19)) for all $\alpha \geq \hat{\alpha}$ (cf. §Appendix B). Crucially, $\tilde{w}(\alpha)$ can be further confirmed to be strictly monotonically decreasing in α (cf. §Appendix D.1.3).

Since $\tilde{w}(\alpha)$ is thus monotonically decreasing on its complete domain $[0, \alpha_{\max}]$, the value range of $\tilde{w}$ for that domain is bounded to $[w^<, w^>]$, where

$$w^< = \tilde{w}(\alpha_{\max}) \overset{(D.5)}{=} \tilde{w}(\alpha^{\leftarrow}(w_1)) = \tilde{w}^{\leftarrow}(w_1) \tag{D.7}$$

$$w^> = \tilde{w}(\alpha_{\min}) \overset{(D.4)}{=} \tilde{w}(\alpha^{\leftarrow}(w_0)) = \tilde{w}^{\leftarrow}(w_0) \tag{D.8}$$

The function $\tilde{w}(\alpha)$ is visualized in Fig. D.18.

Note that the above equation also introduces the function $\tilde{w}^{\leftarrow}(w) = \tilde{w}(\alpha^{\leftarrow}(w))$, which is of great importance throughout the rest of the proof. This function $\tilde{w}^{\leftarrow}$ can be explicitly represented based on Eq. (D.6):

$$\tilde{w}^{\leftarrow}(w) = \begin{cases} w^> & \text{if } w \leq w_0, \\ \tilde{w}(\grave{\alpha}^{\leftarrow}(w)) & \text{if } w \in (w_0, w_1), \\ w^< & \text{if } w \geq w_1, \end{cases} \tag{D.9}$$

where w_0 and w_1 are such that $\tilde{w}^{\leftarrow}$ is *strictly* monotonically decreasing for arguments $w \in [w_0, w_1]$. In summary, the function $\tilde{w}^{\leftarrow}(w)$ is monotonically decreasing for all w:

$$\forall w \in \mathbb{R}. \quad \frac{\partial \tilde{w}^{\leftarrow}(w)}{\partial w} \leq 0 \tag{D.10}$$

Based on Eq. (D.9), we can finally represent $w^{\leftarrow}(w)$. For every interval, $w^{\leftarrow}$ describes the convergence from the interval-start CUBIC window size w towards its associated equilibrium $\tilde{w}(\alpha^{\leftarrow}(w)) = \tilde{w}^{\leftarrow}(w)$, which follows from the asymptotic stability of any $\tilde{w}(\alpha)$ proven in Theorem 2:

$$w^{\leftarrow}(w) \in \begin{cases} (w, \tilde{w}^{\leftarrow}(w)] & \text{if } w < \tilde{w}^{\leftarrow}(w), \\ [w] = [\tilde{w}^{\leftarrow}(w)] & \text{if } w = \tilde{w}^{\leftarrow}(w), \\ [\tilde{w}^{\leftarrow}(w), w) & \text{if } w > \tilde{w}^{\leftarrow}(w). \end{cases} \tag{D.11}$$

The function $\tilde{w}^{\leftarrow}$ and the value ranges for $w^{\leftarrow}(w)$ are illustrated in Fig. D.19.

Appendix D.1.3. Strict monotonic decrease of $\tilde{w}$

To confirm that $\tilde{w}(\alpha)$ is strictly monotonically decreasing for all α, we distinguish the cases $\alpha \geq \hat{\alpha}$ and $\alpha < \hat{\alpha}$.

$\alpha \geq \hat{\alpha}$. First, we note that $\tilde{w} = \tilde{w}^{\max}$ is strictly monotonically increasing in $\tilde{s}$ (Eq. (7)). In turn, $\tilde{s}(\alpha)$ is strictly monotonically decreasing in α if all α_0 and α_1 with $\hat{\alpha} \leq \alpha_0 < \alpha_1$ satisfy:

$$\tilde{s}(\alpha_0) > \tilde{s}(\alpha_1) \impliedby \forall s > s_0(\tau_k).\ \tilde{S}_1(s, \alpha_0) < \tilde{S}_1(s, \alpha_1), \tag{D.12}$$

where $s_0(\tau_k)$ is the lower bound on all roots of polynomial $\tilde{S}_1$ from Theorem 1, given delay τ_k for the CUBIC flow. This lower bound is found by setting $C_\ell = 0$, which yields:

$$\tilde{S}_1(s_0) = \frac{\alpha - 1}{\alpha} \left(\frac{c^2}{b\tau_k} s_0^7 - c s_0^3 \right) \overset{!}{=} 0 \iff s_0 = \sqrt[4]{\frac{b\tau_k}{c}}. \tag{D.13}$$

Returning to Eq. (D.12), we note that

$$\begin{aligned} &\tilde{S}_1(s,\alpha_0) < \tilde{S}_1(s,\alpha_1) \\ \iff &\frac{\alpha_0 - 1}{\alpha_0}\left(\frac{c^2}{b\tau_k}s^7 - cs^3\right) < \frac{\alpha_1 - 1}{\alpha_1}\left(\frac{c^2}{b\tau_k}s^7 - cs^3\right) \end{aligned} \tag{D.14}$$

holds if the s-polynomial in the parentheses is strictly positive, which is again true for all $s > s_0(\tau_k)$. This insight implies $\tilde{s}(\alpha_0) > \tilde{s}(\alpha_1)$ and also $\tilde{w}(\alpha_0) > \tilde{w}(\alpha_1)$, i.e., $\tilde{w}(\alpha)$ is strictly monotonically decreasing for all $\alpha \geq \hat{\alpha}$.

$\alpha < \hat{\alpha}$. The demonstration of strict negative monotonicity for $\alpha < \hat{\alpha}$ works analogously to the previous case, but is based on $\tilde{S}_2$ instead of $\tilde{S}_1$. Intriguingly, we again find $s_0(\tau_k)$ as in Eq. (D.13), marking both the lower bound on possible roots and the lower bound on roots whose position is a strictly monotonically decreasing function of α. Hence, $\tilde{w}$ is a strictly monotonically decreasing function for all α.

Appendix D.2. CUBIC Long-Term Equilibrium Window Size $\overline{w}$

Given the update functions from §Appendix D.1, we can characterize the equilibrium of the discrete dynamic process in Eq. (21). In particular, we will prove the existence and the uniqueness of an equilibrium $\overline{w}$ such that $\overline{w} = w^{\leftarrow}(\overline{w})$. From Eq. (D.11), we learn that $w^{\leftarrow}(w)$ only returns the argument w as a value if $w = \tilde{w}^{\leftarrow}(w)$. Hence, the equilibrium condition can only hold if

$$\overline{w} = \tilde{w}^{\leftarrow}(\overline{w}). \tag{D.15}$$

Since $\tilde{w}^{\leftarrow}$ is monotonically decreasing (Eq. (D.10)), we know that its value range $\mathcal{R}(\tilde{w}^{\leftarrow})$ given argument range $[w^{<}, w^{>}]$ is

$$\mathcal{R}(\tilde{w}^{\leftarrow}) = [\tilde{w}^{\leftarrow}(w^{>}), \tilde{w}^{\leftarrow}(w^{<})] \subseteq [w^{<}, w^{>}] \tag{D.16}$$

where the subset relation holds for the following reason (symmetric for $w^{<}$ and w_0):

$$\begin{aligned} \text{If } w^{>} < w_1: \quad & \tilde{w}^{\leftarrow}(w^{>}) \overset{\text{Eq. (D.10)}}{\geq} \tilde{w}^{\leftarrow}(w_1) \overset{\text{Eq. (D.7)}}{=} w^{<} \\ \text{If } w^{>} \geq w_1: \quad & \tilde{w}^{\leftarrow}(w^{>}) \overset{\text{Eq. (D.9)}}{=} w^{<} \end{aligned} \tag{D.17}$$

In a next step, we consider the fixed-point function $w^*(w) = w - \tilde{w}^{\leftarrow}(w)$. Since any equilibrium $\overline{w}$ must satisfy $\overline{w} = \tilde{w}^{\leftarrow}(\overline{w})$, it must satisfy $w^*(\overline{w}) = 0$. Note that $w^*(w)$ is now *strictly monotonically increasing*. The value range $\mathcal{R}(w^*)$ for argument range $[w^{<}, w^{>}]$ is therefore:

$$\mathcal{R}(w^*) = [w^{<} - \tilde{w}^{\leftarrow}(w^{<}), w^{>} - \tilde{w}^{\leftarrow}(w^{>})]. \tag{D.18}$$

Eq. (D.16) suggests that $w^{<} \leq \tilde{w}^{\leftarrow}(w^{>}) \leq \tilde{w}^{\leftarrow}(w^{<})$ and $w^{>} \geq \tilde{w}^{\leftarrow}(w^{<}) \geq \tilde{w}^{\leftarrow}(w^{>})$. As a result, we find that $w^{<} - \tilde{w}^{\leftarrow}(w^{<}) \leq 0$ and $w^{>} - \tilde{w}^{\leftarrow}(w^{<}) \geq 0$. This finding, together with the continuousness and strict monotonicity of w^*, imply (by the intermediate-value theorem) that a unique $\overline{w} \in [w^{<}, w^{>}]$ exists such that $w^*(\overline{w}) = 0 \iff \overline{w} = \tilde{w}^{\leftarrow}(\overline{w})$. This $\overline{w}$ is thus a unique equilibrium which is guaranteed to exist.

Appendix D.3. Convergence Trajectories

Given the unique equilibrium $\overline{w}$, we now investigate the stability properties of this equilibrium. In other words, we characterize the convergence trajectories determined by the discrete process in Eq. (21), and elicit a condition under which these trajectories may or may not lead to the equilibrium. This stability property depends on the neighborhood of the equilibrium $\overline{w}$ with respect to the update function $w^{\leftarrow}$.

In particular, we now show that the equilibrium $\overline{w}$ is unstable if an equilibrium neighborhood Ω exists such that the window-update function w has a slope of less than -1 in the complete neighborhood:

$$\exists \Omega = (\omega_0, \omega_1),\ \omega_0 < \overline{w} < \omega_1. \quad \forall \omega \in \Omega.\ \frac{\partial w^{\leftarrow}}{\partial w} < -1 \tag{D.19}$$

In other words, we will show that all evolution trajectories from a window size $\omega \in \Omega$ in this neighborhood lead out of the neighborhood. In that case, even if the dynamics outside the neighborhood converge into the neighborhood, the trajectory then leaves the neighborhood again and the equilibrium is not converged upon.

In particular, we consider a state $w(t)$ with $w(t) \in \Omega$ and $w(t) < \overline{w}$ (The proof for $w(t) > \overline{w}$ is symmetric). Since both $w(t)$ and $\overline{w}$ are in Ω, $w^{\leftarrow}$ is strictly monotonically decreasing between $w(t)$ and $\overline{w}$, and therefore

$$w(t) < \overline{w} \implies w(t+1) = w^{\leftarrow}(w(t)) > w^{\leftarrow}(\overline{w}) \overset{\text{(D.15)}}{=} \overline{w}. \tag{D.20}$$

At this point, $w(t+1)$ might already be outside of Ω if $w(t+1) > \omega_1$. Otherwise, if $w(t+1) \in \Omega$, we know by the same argument that $w(t+2) = w^{\leftarrow}(w(t+1)) < \overline{w}$. Again, $w(t+2)$ might be out of the neighborhood Ω if $w(t+2) < \omega_0$.

Importantly, w will *eventually* leave the neighborhood if for all any t, $w(t+2) < w(t)$, i.e., the window state moves away from the equilibrium $\overline{w}$ and will eventually fall below ω_0. This condition can be reformulated:

$$\begin{aligned}
&w(t+2) < w(t) \overset{\text{Expand}}{\iff} w^{\leftarrow}(w^{\leftarrow}(w(t))) < w(t) \overset{-w^{\leftarrow}(w(t))}{\iff} \\
&w^{\leftarrow}(w^{\leftarrow}(w(t))) - w^{\leftarrow}(w(t)) < w(t) - w^{\leftarrow}(w(t)) \\
&\overset{/\text{RHS}}{\underset{\text{RHS} \overset{\text{(D.20)}}{<} 0}{\iff}} \frac{w^{\leftarrow}(w^{\leftarrow}(w(t))) - w^{\leftarrow}(w(t))}{w(t) - w^{\leftarrow}(w(t))} > 1 \\
&\overset{\cdot -1}{\iff} \frac{w^{\leftarrow}(w^{\leftarrow}(w(t))) - w^{\leftarrow}(w(t))}{w^{\leftarrow}(w(t)) - w(t)} < -1.
\end{aligned} \tag{D.21}$$

The last inequality in Eq. (D.21) can be understood as a condition on the average slope of $w^{\leftarrow}$ in $[w(t), w^{\leftarrow}(w(t))]$. Since we are considering the case where both $w(t)$ and $w^{\leftarrow}(w(t))$ are in the neighborhood Ω, the derivative condition in Eq. (D.19) implies this average-slope condition.

Appendix E. Proof of Theorem 4: Maximally intensive oscillation

Appendix E.1. Maximum Oscillation Amplitude

In order to find plausible bounds of the flow-size distribution in BBR-CUBIC competition, we consider the worst case in terms of oscillation amplitude. To characterize this worst-case oscillation amplitude, we make two observations.

Convergence speed. We note that the oscillation amplitude is proportional to the convergence speed of the short-term dynamics in each update interval: In interval $[t, t+1]$, these short-term dynamics involve a CUBIC window-size change from the initial CUBIC window size $w(t)$ to window size $w(t+1) = w^{\leftarrow}(w(t))$, where $w^{\leftarrow}(w(t))$ is between the initial window size $w(t)$ and the short-term equilibrium window size $\tilde{w}^{\leftarrow}(w(t))$. Hence, a high similarity between $w^{\leftarrow}$ and $\tilde{w}^{\leftarrow}$ indicates a high convergence speed, quick window-size changes, and thus a large amplitude of the oscillation. In the following proof, we therefore assume $w^{\leftarrow} = \tilde{w}^{\leftarrow}$ to maximize the oscillation amplitude.

Neighborhood size. We note that the oscillation amplitude is proportional to the size of the unstable neighborhood $\Omega = [\omega_0, \omega_1]$ of the long-term equilibrium window size $\overline{w}$. Since the process $\{w(t)\}_{t \in \mathbb{N}, t \geq 0}$ evolves away from this equilibrium $\overline{w}$ when in neighborhood Ω, the oscillation mostly involves window sizes $w \neq \Omega$ left and right of the neighborhood. Moreover, many steps of the oscillation also need to cross Ω, e.g., change the window size from $w(t) < \omega_0$ to $w(t+1) > \omega_1$. Hence, $\omega_1 - \omega_0$ is proportional to the window-size changes within the update periods, and thus to the oscillation amplitude. Since the update function $w^{\leftarrow}$ (in our case: $\tilde{w}^{\leftarrow}$) must be strictly decreasing in Ω, the maximally large neighborhood $\Omega = (\omega_0, \omega_1)$ corresponds to (w_0, w_1), i.e., the decreasing part of $\tilde{w}^{\leftarrow}$ (cf. Eq. (D.9)).

Appendix E.2. Existence of Limit Cycle

With the two assumptions from §Appendix E.1, we now prove that the BBR-CUBIC oscillation has a limit cycle of CUBIC window sizes $\tilde{w}^{\leftarrow}(w^{<})$ and $\tilde{w}^{\leftarrow}(w^{>})$, i.e., the CUBIC window size persistently alternates between these two values.

Clearly, such a limit cycle only exists given an unstable long-term equilibrium $\overline{w}$. As noted in §Appendix D.3, an equilibrium $\overline{w}$ is only unstable if $\overline{w} \in (w_0, w_1)$ with $w_0 < w_1$, i.e., $\overline{w} = \tilde{w}^{\leftarrow}(\overline{w})$ is a value of $\tilde{w}^{\leftarrow}$ in the decreasing part of $\tilde{w}^{\leftarrow}$. Since the values of $\tilde{w}^{\leftarrow}$ are restricted to $[w^{<}, w^{>}]$ (cf. Eqs. (D.7) and (D.8)), it holds that $\overline{w} \in ([w^{<}, w^{>}] \cap (w_0, w_1)) =: W_{\cap}$. Since $\overline{w}$ is guaranteed to exist, we know that $W_{\cap} \neq \varnothing$, and thus

$$w_0 < w^{>} \quad \text{and} \quad w_1 > w^{<}. \tag{E.1}$$

In the following, we consider all possible cases for $W_{\cap}$, and verify whether the limit cycle is sound, i.e.,:

$$\begin{aligned} \tilde{w}^{\leftarrow}(w^{<}) &= \tilde{w}^{\leftarrow}(\tilde{w}^{\leftarrow}(w^{>})) \\ \tilde{w}^{\leftarrow}(w^{>}) &= \tilde{w}^{\leftarrow}(\tilde{w}^{\leftarrow}(w^{<})) \end{aligned} \tag{E.2}$$

Appendix E.2.1. $W_{\cap} = (w_0, w_1)$

Given the intersection range, we know that $w^{<} \leq w_0 < w_1 \leq w^{>}$. This interleaving implies that

$$\tilde{w}^{\leftarrow}(w^{<}) \overset{(D.9)}{=} w^{>} \quad \text{and} \quad \tilde{w}^{\leftarrow}(w^{>}) \overset{(D.9)}{=} w^{<}. \tag{E.3}$$

Clearly, the limit cycle is sound in this case:

$$\begin{aligned} \tilde{w}^{\leftarrow}(w^{<}) &\overset{(E.3)}{=} \tilde{w}^{\leftarrow}(\tilde{w}^{\leftarrow}(w^{>})) \\ \tilde{w}^{\leftarrow}(w^{>}) &\overset{(E.3)}{=} \tilde{w}^{\leftarrow}(\tilde{w}^{\leftarrow}(w^{<})) \end{aligned} \tag{E.4}$$

Appendix E.2.2. $W_{\cap} = [w^{<}, w_1)$

Given the intersection range, we know that $w_0 < w^{<} < w_1 \leq w^{>}$. Hence, we know that

$$\tilde{w}^{\leftarrow}(w^{<}) \overset{(D.9)}{<} w^{>} \quad \text{and} \quad \tilde{w}^{\leftarrow}(w^{>}) \overset{(D.9)}{=} w^{<}. \tag{E.5}$$

With this knowledge, the first soundness condition in Eq. (E.2) holds:

$$\tilde{w}^{\leftarrow}(w^{<}) \overset{(E.5)}{=} \tilde{w}^{\leftarrow}(\tilde{w}^{\leftarrow}(w^{>})) \tag{E.6}$$

The second condition, however, is not directly satisfied, but can be converted to:

$$\tilde{w}^{\leftarrow}(w^{>}) = \tilde{w}^{\leftarrow}(\tilde{w}^{\leftarrow}(w^{<})) \overset{(E.5)}{\iff} \tag{E.7}$$

$$w^{<} = \tilde{w}^{\leftarrow}(\tilde{w}^{\leftarrow}(w^{<})) \overset{(D.9)}{\iff} \tag{E.8}$$

$$\tilde{w}^{\leftarrow}(w^{<}) \geq w_1 \overset{(D.7)}{\iff} \tilde{w}^{\leftarrow}(\tilde{w}^{\leftarrow}(w_1)) \geq w_1 \tag{E.9}$$

$$\overset{-\tilde{w}^{\leftarrow}(w_1)}{\iff} \tilde{w}^{\leftarrow}(\tilde{w}^{\leftarrow}(w_1)) - \tilde{w}^{\leftarrow}(w_1) \geq w_1 - \tilde{w}^{\leftarrow}(w_1)$$

$$\overset{(D.9)}{=} w_1 - w^{<} \overset{(E.1)}{>} 0 \tag{E.10}$$

$$\overset{/\text{RHS}}{\underset{\cdot -1}{\iff}} \frac{\tilde{w}^{\leftarrow}(\tilde{w}^{\leftarrow}(w_1)) - \tilde{w}^{\leftarrow}(w_1)}{\tilde{w}^{\leftarrow}(w_1) - w_1} \leq -1 \tag{E.11}$$

In turn, the last condition on w_1 is ensured by the derivative condition in neighborhood $\Omega = [w_0, w_1]$, i.e., by Eq. (D.19).

Appendix E.2.3. $W_\cap = (w_0, w^>]$

This case is symmetric to the case for $W_\cap = [w^<, w_1)$ since $w^< \leq w_0 < w^> < w_1$.

Appendix E.2.4. $W_\cap = [w^<, w^>]$

From the intersection range, we derive $w^< > w_0$ and $w^> < w_1$. These conditions can be shown to be incompatible with an unstable equilibrium (again via the derivative condition):

$$w^> - w^< < w_1 - w_0 \overset{\substack{/\text{RHS} \\ \cdot -1}}{\Longleftrightarrow} \frac{\tilde{w}^{\leftarrow}(w_0) - \tilde{w}^{\leftarrow}(w_1)}{w_0 - w_1} > -1. \tag{E.12}$$

Hence, this case is outside the scope of this proof.

Appendix E.3. Convergence to Limit Cycle

In the following, we show that the long-term dynamics of the CUBIC window size w converge to the limit cycle constituted by $\tilde{w}^{\leftarrow}(w^<)$ and $\tilde{w}^{\leftarrow}(w^>)$. For this purpose, we revisit all relevant cases from §Appendix E.2.

Appendix E.3.1. $W_\cap = (w_0, w_1)$

Without loss of generality, we assume an initial state $w(t) < \overline{w}$, which allows the following case distinction:

- $\boldsymbol{w(t) \leq w_0}$: We know that $w(t+1) = \tilde{w}^{\leftarrow}(w(t)) \overset{(D.9)}{=} w^>$. Hence, the limit cycle is entered in the first step, as $w^>$ is part of the limit cycle by Eq. (E.3).
- $\boldsymbol{w(t) \in (w_0, \overline{w})}$ **:** We note that $\tilde{w}^{\leftarrow}$ is strictly monotonically decreasing between $w(t) > w_0$ and $\overline{w} < w_1$ by Eq. (D.9), and thus

$$w(t+1) = \tilde{w}^{\leftarrow}(w(t)) > \tilde{w}^{\leftarrow}(\overline{w}) \overset{(D.15)}{=} \overline{w}. \tag{E.13}$$

  - $\boldsymbol{w(t+1) \geq w_1}$: The limit cycle is entered at $w(t+2) = \tilde{w}^{\leftarrow}(w(t+1)) = w^<$, as $w^<$ is part of the limit cycle by Eq. (E.3).
  - $\boldsymbol{w(t+1) \in (\overline{w}, w_1)}$: We again note that $\tilde{w}^{\leftarrow}$ is strictly monotonically decreasing between $\overline{w} > w_0$ and $w(t+1) < w_1$, and thus $w(t+2) = \tilde{w}^{\leftarrow}(w(t+1)) < \overline{w}$. Moreover, the window size makes progress towards the limit cycle if $w(t+2) < w(t)$, which can once more be guaranteed via the derivative condition.

Appendix E.3.2. $W_\cap = [w^<, w_1)$

In this case, the limit cycle L is composed of $w^<$ and $\tilde{w}^{\leftarrow}(w^<) < w^>$ (Eq. (E.5)). Without loss of generality, we assume an initial state $w(t) < \overline{w}$, which allows the following case distinction:

- $\boldsymbol{w(t) \leq w_0}$: In that case, $w(t+1) = \tilde{w}^{\leftarrow}(w(t)) = w^>$ by Eq. (D.9). Since $w^> \geq w_1$ in the current case, the limit cycle is entered at $w(t+2) = \tilde{w}^{\leftarrow}(w^>) = w^<$.
- $\boldsymbol{w(t) \in (w_0, w^<)}$: We note that $\tilde{w}^{\leftarrow}$ is strictly monotonically decreasing between $w(t) > w_0$ and $w^< \leq w_1$ (Eq. (D.9)), where $w(t) < w^<$. This property implies that

$$w(t+1) = \tilde{w}^{\leftarrow}(w(t)) > \tilde{w}^{\leftarrow}(w^<) \overset{(E.10)}{\geq} w_1. \tag{E.14}$$

  Since $w(t+1) \geq w_1$, the limit cycle is then entered at $w(t+2) = \tilde{w}^{\leftarrow}(w(t+1)) = w^<$.
- $\boldsymbol{w(t) \in [w^<, \overline{w})}$: This case only arises if $w^< < \overline{w}$. Hence, $\tilde{w}^{\leftarrow}$ is again strictly monotonically decreasing between $w^< > w_0$ and $\overline{w} < w_1$, and therefore $w(t+1) > \overline{w}$ from Eq. (E.13) holds again.
  - $\boldsymbol{w(t+1) \geq w_1}$: The limit cycle is entered at $w(t+2) = \tilde{w}^{\leftarrow}(w(t+1)) = w^<$ by Eq. (D.9).
  - $\boldsymbol{w(t+1) \in (\overline{w}, w_1)}$: Based on arguments symmetric to the above analysis, plus the derivative condition from Eq. (D.19), we find that $w(t+2) \in [w^<, w(t))$, which implies that the limit cycle is eventually entered.

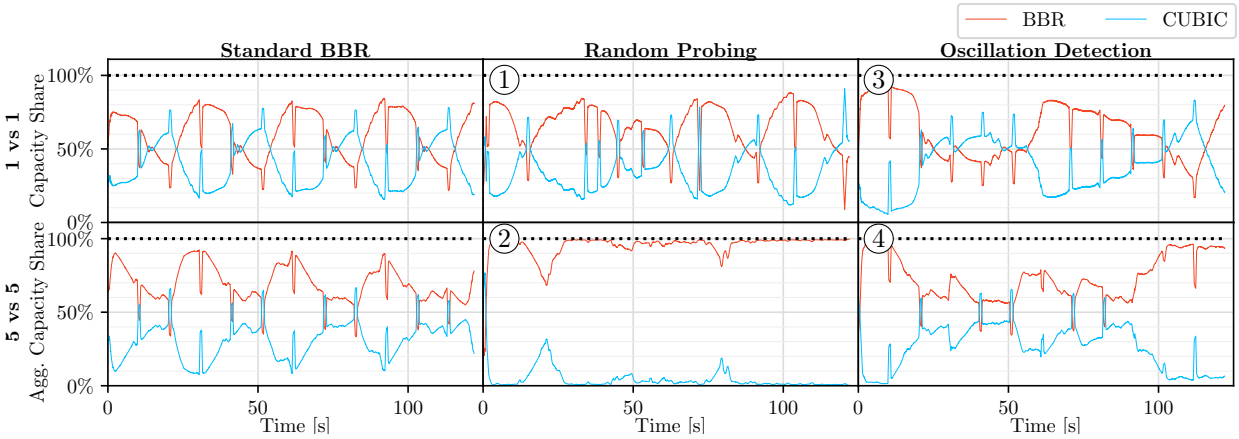

Figure F.20: Evaluation of two strategies for oscillation suppression. 'Random Probing' desynchronizes RTT-probing steps, and 'Oscillation Detection' freezes min-RTT estimate at high estimate variance.

Appendix E.3.3. $W_{\cap} = (w_0, w^{>}]$

This case is symmetric to the case in §Appendix E.3.2 (directly above).

Appendix F. Derivation of Non-Pessimal Fairness Bounds

Fundamentally, we note that the evolution of the CUBIC congestion-window size w is controlled by the CUBIC window-growth function $W(w^{\max}, s)$ from Eq. (1).

The first argument of W, i.e., the recorded maximum window $w^{\max}$, converges sub-exponentially, i.e., slowly, to its current short-term equilibrium value $\tilde{w}^{\max}$, as both the proof of Theorem 2 and the visualization in Fig. 7 demonstrate. The short-term equilibrium values $\tilde{w}^{\max}$ themselves alternate between values above and below the long-term equilibrium $\overline{w}^{\max} = \overline{w}$, which is implied by the structure of the function $\tilde{w}^{\leftarrow}$ (Fig. 8) and the fact $\tilde{w}^{\max} = \tilde{w}$ for any short-term equilibrium (Eq. (7)). Given slow convergence in alternating directions, it is plausible that $w^{\max}$ is usually close to the intermediate value $\overline{w}^{\max} = \overline{w}$, i.e., the long-term equilibrium. Hence, we assume $w^{\max} = \overline{w}$ for the non-pessimal bound.

Given this fixed first argument of W, we derive the non-pessimal bounds from the variance in the second argument, the window-growth duration s. Clearly, the minimum possible value of s is 0, leading to the maximum non-pessimal bound $\phi^{\mathrm{B}}(\hat{W}_0)$ of the BBR capacity share, where

$$\hat{W}_0 = W(\overline{w}, 0) = \overline{w} + c \cdot \left(-\sqrt[3]{\frac{b}{c}\overline{w}} \right)^3 = (1-b)\overline{w}. \tag{F.1}$$

Conversely, the window-growth duration s (and thus also the CUBIC window size w) attains its highest value if it grows without interruption for the entire 10 seconds between RTT-probing steps. In fact, s rarely grows beyond a total of 10 seconds in realistic settings, as s causes rapid growth in the CUBIC congestion-window size w, which quickly leads to loss and thus resets s. More formally, the maximum possible short-term equilibrium value $\tilde{s}(\alpha_{\min}) = \tilde{s}(2\tau^{\mathrm{p}}/\overline{\tau})$ is below 10 seconds for all settings in Fig. 11. While s can temporarily exceed this equilibrium value during its evolution (Fig. 7), the proof of Theorem 2 confirms that s converges exponentially fast to its short-term equilibrium value $\tilde{s}$, suggesting that s never grows much beyond $\tilde{s}$. In summary, assuming a maximum s of 10 seconds leads to the minimum non-pessimal bound $\phi^{\mathrm{B}}(\hat{W}_1)$ for the BBR capacity share, where

$$\hat{W}_1 = W(\overline{w}, 10) = \overline{w} + c \cdot \left(10 - \sqrt[3]{\frac{b}{c}\overline{w}} \right)^3. \tag{F.2}$$

Appendix G. Evaluation of Further BBR Modifications

As explained in §3.2, BBR/CUBIC oscillation happens because the BBR flows simultaneously perform RTT probing by briefly, but sharply reducing their rate. Therefore, the BBR flows regularly estimate a relatively low minimum RTT, especially if the CUBIC flows are small at the time of probing. This low minimum-RTT estimate then decreases the BBR sending rate (via the BBR congestion window), increases the CUBIC sending rate, and thus leads to a higher minimum-RTT estimate at the next RTT probing. If that next minimum-RTT estimate is high enough, the evolution of the sending rates is reversed, causing oscillation.

This causal chain may be disrupted by a number of possible modifications to the BBR algorithm, which we discuss and experimentally evaluate in the following.

Randomize RTT probing. As described above, oscillation requires that all BBR flows simultaneously perform RTT probing, namely every 10 seconds. If these RTT-probing periods were randomized, each flow would probe the RTT when other BBR flows still contribute to the queue. Hence, the high minimum-RTT estimates would be consistently high rather than varying over time. While such randomization might avoid oscillation, it is undesirable for three reasons.

First, the synchronization of the RTT probing among BBR flows is a conscious feature of BBR, enabling BBR flows to discover the path propagation delay in a pure BBR scenario; this discovery would be prevented by randomization. Second, randomization does not prevent oscillation given a single BBR flow, as visible in Fig. F.20 ①. Given a single BBR flow, no other BBR flows exist that could inflate the minimum-RTT estimate. Hence, the rate of the randomized single BBR flow still oscillates, although not in 10-second steps anymore, but in intervals with varying duration. Third, randomization can suppress oscillation only at the cost of even lower fairness, as the experiment in Fig. F.20 ② demonstrates: Since randomization causes consistently high minimum-RTT estimates, it also causes consistently high BBR rates and near-starvation of the CUBIC flows.

Detect oscillation and freeze. To suppress oscillation in a more targeted fashion, we envision that a BBR flow (i) keeps a recent history of its minimum-RTT estimates, (ii) maintains the mean μ and the standard deviation σ of these estimates, and (iii) concludes that oscillation is ongoing if the standard deviation σ exceeds a configured share κ of the mean μ. In case of oscillation, the BBR flow then considers μ its minimum-RTT estimate.

Unfortunately, this oscillation-suppression strategy is self-defeating: When oscillation is suppressed for a sufficiently long time, the variance of minimum-RTT estimates decreases, the oscillation-suppression mechanism is deactivated, and oscillation resumes. Hence, this mechanism does not eliminate the oscillation, but only prolongs the oscillation period (see experiments ③ and ④ in Fig. F.20). Moreover, the mechanism relies on a suitable value κ to distinguish structural oscillation from acceptable fluctuation of the minimum-RTT estimates, which might be difficult to find in practice.